Biomaterials 309 (2024) 122598

Contents lists available at ScienceDirect

Biomaterials

journal homepage: www.elsevier.com/locate/biomaterials

Transformation of metallo-elastomer grafts in a carotid artery interposition model over a year

Ying Grace Chen [a,1], Catia Dombaxe [a], Anthony Richard D'Amato [a], Simon Van Herck [a], Halle Welch [a], Qin Fu [b], Sheng Zhang [b], Yadong Wang [a,*]

[a] Meinig School of Biomedical Engineering, Cornell University, Ithaca, NY, 14850, USA
[b] Proteomics and Metabolomics Facility, Institute of Biotechnology, Cornell University, Ithaca, NY, 14850, USA

ARTICLE INFO

Keywords:
Vascular graft
Metal-ligand chelation
Biodegradable elastomer
Artery tissue engineering
Carotid artery
Bioinformatics

ABSTRACT

Current vascular grafts, primarily Gore-Tex® and Dacron®, don't integrate with the host and have low patency in small-diameter vessels (<6 mm). Biomaterials that possess appropriate viscoelasticity, compliance, and high biocompatibility are essential for their application in small blood vessels. We have developed metal ion cross-linked poly(propanediol-*co*-(hydroxyphenyl methylene)amino-propanediol sebacate) (M-PAS), a biodegradable elastomer with a wide range of mechanical properties. We call these materials metallo-elastomers. An initial test on Zn-, Fe-, and Cu-PAS grafts reveals that Cu-PAS is the most suitable because of its excellent elastic recoil and well-balanced polymer degradation/tissue regeneration rate. Here we report host remodeling of Cu-PAS vascular grafts in rats over one year. 76 % of the grafts remain patent and >90 % of the synthetic polymer is degraded by 12 months. Extensive cell infiltration leads to a positive host remodeling. The remodeled grafts feature a fully endothelialized lumen. Circumferentially organized smooth muscle cells, elastin fibers, and widespread mature collagen give the neoarteries mechanical properties similar to native arteries. Proteomic analysis further reveals the presence of important vascular proteins in the neoarteries. Evidence suggests that Cu-PAS is a promising material for engineering small blood vessels.

1. Introduction

Cardiovascular diseases are a major cause of mortality and morbidity, accounting for approximately 700,000 American deaths in 2020 [1]. There are about 500,000 coronary and 160,000 peripheral artery bypass surgeries annually, demonstrating the pressing need for viable vascular grafts. The gold standard for vascular graft is autologous vessels, such as the saphenous vein or radial artery, the harvest of which necessitates an additional invasive procedure. For patients with complications like diabetes or calcification, this may not be viable [2]. Alternatively, synthetic grafts, made from materials like Gore-Tex® (expanded polytetrafluoroethylene; ePTFE) or Dacron® (woven polyethylene terephthalate), are often used [3]. Yet, despite their frequent clinical application, these synthetic materials – non-resorbable, with a stiffness roughly 100 times stiffer than native arteries and characterized by low porosity – often fail to integrate with the host tissue and may lead to fibrous encapsulation, chronic inflammation, restenosis, and aneurysm formation [4]. Particularly for small-diameter vessels under 6 mm, these grafts have shown high failure rates due to thrombogenicity and intimal hyperplasia [5], driving the pursuit of more efficacious materials.

Emerging research is now investigating the potential of resorbable vascular grafts, which are acellular and utilize the advantage of *in situ* implantation [6]. These grafts facilitate host cells to infiltrate, proliferate, degrade polymers, synthesize new matrix, and eventually remodel the grafts to a completely autologous conduit. Resorbable grafts also offer benefits such as ease of storage, high uniformity, minimal immunogenicity, and lower cost. Notably, they avoid the challenges associated with cell or tissue harvest. A vital aspect of these resorbable grafts is balancing graft material degradation with neotissue regeneration. The rate of degradation must strike a balance between providing mechanical support during the initial healing period and allowing for host cell infiltration and new tissue formation. Rapid degradation may lead to premature mechanical failure, while overly slow degradation may

* Corresponding author. Meinig School of Biomedical Engineering, Cornell University, 277 Kimball Hall, Ithaca, NY, 14853, USA.
E-mail address: yw839@cornell.edu (Y. Wang).
[1] Current address: Cardiovascular Institute, Rowan-Virtua School of Translational Biomedical Engineering & Sciences, Rowan University, Camden, NJ 08103, USA., and Biomedical Engineering, Henry M. Rowan College of Engineering, Rowan University, Glassboro, NJ 08028, USA.

https://doi.org/10.1016/j.biomaterials.2024.122598
Received 10 March 2024; Received in revised form 24 April 2024; Accepted 26 April 2024
Available online 26 April 2024

impede new tissue formation or cause complications [7].

Various resorbable polymers have been investigated for vascular graft applications. The poly(lactic acid)/poly(glycolic acid) (PLA/PGA) family, for instance, either degrade too slowly (PLA) or too quickly (PGA) [8–10]. Copolymers like poly(lactic-*co*-glycolic acid) (PLGA), despite their tunable degradation rates, pose concerns due to their acidic degradation products [11]. Polycaprolactone (PCL) is known for its cytocompatibility but faces challenges due to its supraphysiologic moduli, potential for calcification, and inconsistent quality [12]. Concerns are particularly pointed at PCL's slow degradation rate. The two to four years complete degradation window [13], while allowing sufficient time for host tissue development and scaffold replacement by the host's own tissue [14], can lead to extended inflammation and cellular infiltration regression [12]. Polydioxanone (PDO) degrades faster, leading to risks of aneurism. It shows cessation of neotissue formation coincided with full material loss [15]. Certain degradable polyurethanes, such as poly(ester urethane)urea (PEUU), poly(ether urethane) (PEU), and poly (carbonate urethane) (PCU) are also limited in cardiovascular applications due to their mismatched degradation rate, biocompatibility, endothelization, long-term stability, and calcification [16]. Despite the limitations observed in these biodegradable vascular grafts, they have provided invaluable insights for the next generation of vascular graft design. A notable development came with poly(glycerol sebacate) (PGS) in the early 2000s [17]. The vascular grafts made from PGS showed similar performance to an autologous vein in a rat carotid artery interposition model for 90 days after implantation [18]. While these results were promising, PGS grafts exhibited rapid degradation in the sheep carotid artery model [19]. This is consistent with what others have observed in the relatively faster degradation of synthetic grafts in sheep vs. rodents [20].

This discovery led to the creation of a novel polymer, poly(propanediol-*co*-(hydroxyphenyl methylene)amino-propanediol sebacate) (PAS), synthesized via polycondensation of 1, 3-propanediol, sebacic acid, and a Schiff-base ligand. Unique to PAS is the ability of its salicylaldimine side groups to chelate metal ions, creating crosslinked M-PAS elastomers with a three-dimensional network structure. By tuning the metal/ligand ratio, ligand density in polymers, metal ion type, and mixing different metal ions, we can modulate the degradation rates, mechanical properties, and functions of the resultant M-PAS elastomers [21].

Once a fully resorbable graft is completely remodeled, no foreign material will remain to induce the chronic inflammation commonly associated with today's synthetic grafts - a common cause of other, well reported-on, long-term complications [22]. In this study, we explored the suitability of M-PAS elastomers as the base material of resorbable small-diameter vascular grafts. We initially determined the most suitable metal ion by evaluating the balance between degradation and tissue regeneration rates. With a 12-month observation window, we scrutinized the long-term performance of the vascular grafts in a rat carotid artery interposition model, focusing on graft patency, degradation, cellular infiltration, inflammation, mechanical properties, and neovessel structure. Through this holistic assessment, our study aims to explore the viability of resorbable M-PAS vascular grafts as pioneering synthetic solutions with the promise to transform into autologous vascular conduits.

2. Materials and methods

2.1. In vitro cytocompatibility study

The *in vitro* cytotoxicity assay was performed on the Cu-PAS coating according to the method detailed in our previous study [21]. 1 % w/v of Cu-PAS in acetone was prepared and 20 μL of the solution was evenly spread on each of the coverslips (12 mm in diameter). 20 μL of 1 % w/v acetone solution of poly(D, L-Lactide-*co*-Glycolide) (PLGA, 50:50, ester terminated, Mw 7000–17,000, Sigma-Aldrich) was coated on each of the coverslips to prepare the controls. The Cu-PAS and PLGA coatings with a thickness of approximately 200 nm were formed on the coverslips. After air-drying and curing, the coverslips were sterilized, treated with ethanol to remove residuals. 5×10^3 Human umbilical vein endothelial cells (HUVECs, C2519A, Lonza), in 20 μL of endothelial cell growth medium (EGM-2 BulletKit, CC-3156 & CC-4147, Lonza), was added dropwise onto the coverslips and the cells were allowed to attach for 3 h before 1 mL of medium was added to each well of the cell culture plates. The cells were incubated at 37 °C with 5 % CO_2. Medium changes every 48 h. Cell metabolic activity was evaluated on days 1, 3, and 6 using an MTT assay (Invitrogen, CA), with absorbance measured by a microplate reader (SpectraMax M3). Live/dead assay was performed after cells incubated for 6 days using a LIVE/DEAD® Viability/Cytotoxicity Kit (Invitrogen, CA). The fluorescence microscopy images were recorded using a Nikon ECLIPSE Ti fluorescence microscope (Nikon Instruments Inc., NY). At day 6, phase-contrast images were also taken for both the Cu-PAS and PLGA wells on a Zeiss Axiovert 200 microscope equipped with a Dage 240 digital camera. All experiments were performed in triplicate.

2.2. M-PAS vascular grafts preparation

The grafts were fabricated via porogen leaching of poly(methyl methacrylate) (PMMA, Cospheric LLC) beads. First, a custom cylindrical glass mold (inner diameter = 2.0 mm, length = 15 mm), equipped with a central stainless-steel mandrel (outer diameter = 1.1 mm), was filled with PMMA microspheres (38–45 μm in diameter). The 1.1 mm central mandrel was selected to match the lumen of the native rat carotid artery. To achieve compact bead packing, the bead-filled mold underwent a 30-min sonication process. Thereafter, a heat treatment at 175 °C for 24 h was administered to partially fuse the beads [23]. The fused PMMA microsphere template was then removed from the mold. Anhydrous copper chloride ($CuCl_2$, VWR International) in ethanol, zinc acetate dihydrate ($Zn(AcO)_2{\cdot}2H_2O$, Macron Fine Chemicals) in methanol, or iron chloride hexahydrate ($FeCl_3{\cdot}6H_2O$, Sigma-Aldrich) in ethanol, was added to PAS polymer (300 mg mL^{-1} in a 2:1 mixture of ethanol: 1,4 dioxane) to obtain the M-PAS solution. The molar ratio of the PAS ligand to metal ions was 2. The ligand density of the PAS polymer was calculated based on the ^1H NMR spectra.

The M-PAS polymer solution was then added dropwise on the PMMA templates, followed by heating at 150 °C for 6 h. The M-PAS/PMMA tubes were washed on a shaker at ~50 rpm using a series of ethanol: acetone mixtures followed by full submersion in dichloromethane for 7 days, refreshing the solvent every 8 h to dissolve the PMMA beads. Next, grafts were washed sequentially in acetone, ethanol, and water for 24 h each, refreshing the solvent every 6 h. After freeze-drying, the grafts were sterilized with ethylene oxide (Andersen Products), treated with gas plasma (Harrick Plasma Generator) for 5 min, and immersed in a sterile heparin solution (180 units mL^{-1}) overnight before *in vivo* implantation [24].

2.3. Graft characterization

The microstructures of the grafts were examined using a field emission scanning electron microscope (FESEM, Mira3, Tescan). For imaging, samples (n = 4) were cut into 3 mm-long segments or cross-sections and coated with a layer of gold-platinum using a sputter-coating technique. To visualize the microstructures of the grafts in three dimensions (3D), nano-scale X-ray computed tomography (Nano-CT, Xradia XRM CT instrument) scanning was employed. Samples measuring 2.5 mm in length were scanned at a resolution of 3.06 μm per pixel, and 3D images were reconstructed using Avizo 2.0 software. The mechanical properties of the vascular grafts were evaluated using a material testing system (Instron, Model 5943) equipped with a 50 N static load cell. The dimensions of the samples were measured by an electronic digital caliper (Neiko). Prior to testing, all samples were soaked in DPBS. A uniaxial

force was applied to the grafts until failure occurred. Each group was tested using four different samples (n = 4). The strain and stress of each sample were recorded to generate a stress-strain curve. The testing process was conducted within a short time frame to ensure the samples remained wet. From the acquired stress-strain curve, the linear elastic modulus, ultimate tensile stress (UTS), and strain at break were calculated. The elastic modulus was calculated from the low-strain region (<20 % strain) of the stress-strain curve.

The suture retention force of the grafts was assessed using the same aforementioned material testing system. All test samples were 10 mm in length. A single 9-0 Nylon suture (ARO Surgical) was passed through the specimen, positioned 1 mm from the top edge. The upper clamp of the testing machine held the suture, while the lower clamp secured the non-sutured end of the test sample. The suture was pulled at a constant rate of 50 mm min^{-1}. All grafts were tested under wet conditions at room temperature. The suture retention force was defined as the maximum force recorded before the suture became dislodged from each sample. For each group, four different samples (n = 4) were tested.

Grafts were immersed in a solution of sodium hydroxide (NaOH) for accelerated *in vitro* degradation testing. Prior to treatment with the alkaline solution, the lyophilized samples were weighed to determine their initial weight. Subsequently, each graft was submerged in 5 mL of 60 mM NaOH solution (pH 12.87, prepared in deionized water) and maintained at 37 °C. After 4, 24, or 48 h, the samples were removed from the solution, rinsed with deionized water, lyophilized, and weighed to record any changes in weight. The extent of degradation was quantified by calculating the percentage of weight loss for each sample. For each group and at each time point, the degradation test was conducted using three separate specimens (n = 3).

2.4. Vascular graft implantation

All experimental procedures were approved by the Institutional Animal Care and Use Committee at Cornell University (Protocol Number: 2017–0018), following National Institutes of Health (NIH) guidelines for the ethical care and use of laboratory animals. A total of 47 male Sprague Dawley IGS rats (Charles River Laboratories, Boston, MA) were used for the left common carotid artery interposition of vascular grafts. The right common carotid of the same animal served as the unoperated control. All rats were between 10 and 12 weeks old, with a body weight ranging from 350 to 400 g. 9 rats were used for Zn-PAS graft implantation, 12 for Fe-PAS graft implantation, and 26 for Cu-PAS graft implantation.

Rats were anesthetized by isoflurane, delivered at an initial concentration of 3.0 % isoflurane in 1 L min^{-1} oxygen for induction, followed by a maintenance concentration of 1.5 %. A midline incision was made in the neck, followed by exposure of the left common carotid artery. Carotid blood flow was stopped using double microvascular clamps (Fine Science Tools). An 8-mm segment of the common carotid artery was excised. Grafts were implanted between the two carotid stumps using an end-to-end anastomosis with simple interrupted 10–0 polyamide monofilament sutures (ARO Surgical, Newport Beach). After anastomosis, blood flow was restored by removing the microvascular clamps. The surgical incision was closed using 3-0 MONOCRYL absorbable sutures (Y344H, Ethicon Y). No anticoagulation or antiplatelet treatments were administered in the postoperative period. Ethiqa XR (buprenorphine extended-release injectable suspension, 0.65 mg kg^{-1} body weight, Fidelis Pharmaceuticals, LLC) was injected subcutaneously prior to operation at a dosage of. Each injection of Ethiqa XR provides analgesia for a duration of 72 h.

2.5. Patency monitoring with ultrasonography

To monitor the blood flow and inner diameter of implanted grafts, VisualSonics Vevo-2100 High-Resolution Ultrasound was used 4 days, 1 month, 4 months, 8 months, and 12 months after implantation. The contralateral CCA was monitored as a control. Rats were positioned on a custom-built platform equipped with a warming pad and were anesthetized with 1–2% isoflurane in 1 L min^{-1} oxygen. Prior to ultrasound imaging, the hair in the neck area was removed using a hair removal cream (Nair), and ultrasound gel (AccuGel, Lynn Medical, Wixom, MI) was applied to the skin. Transcutaneous ultrasound imaging of the neck was performed using a linear array transducer (MS 400) centered at 30 MHz. B-mode, color Doppler mode, and pulse wave (PW) mode images were acquired along the long axis of the grafts and native carotids. The patency of the implanted grafts was assessed by the images obtained from the color Doppler mode. The inner diameter of the grafts was estimated by averaging the measurements obtained from the end-diastolic and end-systolic phases in the B-mode images. The diameter was then compared to that of the contralateral arteries. The velocity of peak flow within the implanted grafts was directly extracted from the PW mode image waveform. The velocity of peak flow in the contralateral arteries was used for comparison.

2.6. Histological and immunohistochemical analysis

At 4 days, 1 month, 4 months, 8 months, and 12 months after graft implantation, rats were anesthetized, and the implanted vascular grafts were exposed by creating a midline incision on the neck. The grafts were carefully dissected from the surrounding tissues, then rinsed with 180 units mL^{-1} heparin saline solution, followed by fixation in 4 % paraformaldehyde (Electron Microscopy Sciences) at 4 °C for 2 h. Subsequently, the grafts were soaked in a 30 % sucrose solution at 4 °C for 24 h. Arterial explants were then embedded in optimal cutting temperature compound (OCT, Sakura Finetek), rapidly frozen at −80 °C, and cryosectioned into 8 μm thick slices. These sections were sent to the histology laboratory at the Animal Health Diagnostic Center at Cornell University for staining, including hematoxylin and eosin (H&E), Masson's trichrome, Verhoeff elastin, Picro-sirius red, Alizarin red, as well as immunohistochemical (IHC) staining for calponin and von Willebrand Factor (vWF). The antibodies used for IHC staining were summarized in Table S1, Supplementary Information. A counterstain of hematoxylin was applied to the nuclei for 5 min. All histological images were representative of four independent sections per group (n = 4) and captured with an inverted fluorescence microscope (Eclipse Ti2, Nikon) in brightfield or under polarized light for Picro-sirius red. H&E images from four different samples (n = 4) for each group at the designated time points were used to quantify the luminal area, thickness of graft walls, and percent cell infiltration. The radius of grafts was first calculated through the circumference of the lumen and the luminal area was then calculated from the radius. The thickness of graft walls was the thickness of media and intima layers and was calculated as the average wall thickness of grafts at six random spots. Host cells not only infiltrated into the porous graft, but also assembled into autologous tissue layers on both the luminal and the abluminal side of the graft. The quantification of cell infiltration percentage involved counting the cells within the walls of the native CCA and graft samples, normalizing the counts to the total area of each sample to obtain cell density. The cell density of the native CCA represents a baseline of 100 % infiltration. Then, each graft's cell density was calculated as a percentage relative to this baseline. This percentage reflects the cell infiltration level of the grafts compared to the native artery.

2.7. Immunofluorescence staining

Tissue sections (thickness: 8 μm) were initially fixed with 4 % paraformaldehyde for 1 h at 4 °C and permeabilized with 0.2 % Triton X-100 for 5 min at room temperature. Tissue sections were blocked with 5 % normal goat serum (NGS, Sigma-Aldrich) for 1 h at room temperature. The sections were then incubated overnight at 4 °C with primary antibodies in 1 % NGS. After rinsing with PBS, the samples were exposed to secondary antibodies in 1 % NGS for 1 h at 37 °C. The specific antibodies

used in the experiment are listed in Table S1, Supplementary Information. Nuclei were counterstained for 5 min with 1 μg mL^{-1} (w/v in DI water) of 4', 6-diamidino-2-phenylindole (DAPI, Krackeler Scientific). Tissue sections without primary antibody treatment served as negative controls. The stained samples were visualized using an inverted fluorescence microscope. Four different samples (n = 4) of each group were quantified at the designated time points. ImageJ software was used to quantify the area of cells positively stained by the inflammatory cell markers and the area positive for DAPI staining in the samples. The percentage of positively stained cells was determined by calculating the ratio between the area of positively stained cells and the area positive for DAPI staining. This analysis was performed on fluorescent images from four different samples from each group, resulting in a total of four replicates (n = 4) per group. To avoid interference from the graft polymer, which scatters light in the same channel, all graft areas were excluded from cell quantification.

2.8. Endothelial cell examination at the lumen

For 12-month explants, grafts and native carotids were removed and cut open longitudinally using microscissors. They were then fixed in place with small pins. For SEM imaging, the samples were fixed in 2.5 % glutaraldehyde for 2 h at room temperature, rinsed with PBS, and dehydrated using a series of graded ethanol solutions. After lyophilizing, the samples were sputter coated with a layer of gold and examined via field emission SEM. For en-face immunofluorescence staining, the samples were fixed with 4 % paraformaldehyde for 1 h and permeabilized with 0.2 % Triton X-100 for 5 min at room temperature. Subsequently, the samples were blocked with 5 % NGS for 1 h at 37 °C. They were then incubated with mouse anti-CD31 primary antibody (1:200, Abcam), followed by incubation with Alexa Fluor 594 goat anti-mouse IgG (1:400) secondary antibody. Nuclei were counterstained for 5 min with 1 μg mL^{-1}, of DAPI. Immunofluorescence images were captured using a multiphoton microscope (LSM880 confocal multiphoton inverted-i880, Zeiss).

2.9. En-face imaging of collagen and elastin fibers

Small samples (3 mm length) were excised from all 12-month artery and graft explants(n = 4) and cut open longitudinally using a microscissor. Samples were hydrated with saline, positioned on glass sides, and covered with coverslips. Samples were imaged using a multiphoton microscope (LSM880 confocal multiphoton inverted-i880, Zeiss). The excitation wavelength was set to 800 nm and a C-Apochromat 40x/1.2 W water immersion objective was used for all samples. The second harmonic generation (SHG) signal of collagen was detected at 400 nm (Channel 1). The channel 1 detector has a 720 nm SP excitation filter, a T412/pxr dichroic mirror, and D390/65 barrier filter combination. The elastin autofluorescence was detected at 505–545 nm (Channel 3). The channel 3 detector has a 720 nm SP excitation filter, a T556/pxr dichroic mirror, and Zeiss 525/50 barrier filter combination. Planer images were taken starting either from the outer wall (for collagen) or the inner wall (for elastin), moving in 0.33 μm increments. Z-stacks of ~150 slices were taken. Digital imaging acquisition software was Zen 2012 (Zeiss).

2.10. Mechanical evaluation

The circumferential mechanical properties of the 12-month explants were evaluated using a customized inflation testing device [18]. The explanted grafts were securely mounted on the device by suturing their two ends onto two 25G parallel blunt needles. One end of the device was connected to a syringe pump, which infused PBS at a rate of 60 μL min^{-1}, while the other end was connected to a pressure monitor (Living Systems) to record luminal pressure. The device was equipped with an LS-7601 laser micrometer to measure the outer diameter of the grafts in response to increasing pressure. All data were collected using a data acquisition system (PowerLab 8/30, ADInstruments, Colorado Springs) and the associated software LabChart 7.0. Normalized pressure-stretch curves were plotted. The compliance (%/100 mmHg) was calculated using equation (1) and expressed as the percent diameter change per 100 mmHg.

$$C = \frac{\frac{D_{high} - D_{low}}{D_{low}}}{P_{high} - P_{low}} \times 10,000 \quad (1)$$

To measure the burst pressure of the 12-month explanted grafts and native carotids, PBS was infused into the grafts at a rate of 5 mL min^{-1} until the grafts burst. The same testing apparatus was used but with a pressure transducer capable of measuring higher pressure ranges (0–5000 mmHg, PX309-100G5V, Omega Engineering Inc.). This allowed for accurate burst pressure determination and a comparison between the explanted grafts and native carotid arteries.

2.11. Decellularization and protein extraction for proteomic analysis

12-month graft (n = 3) and contralateral carotid artery (n = 3) explants were dissected, washed, and minced into <1 mm^3 pieces. All samples underwent freezing before lyophilization and were then cryomilled using a Freezer mill 6770 (Spex® SamplePrep LLC) and frozen at −80 °C. For decellularization, samples were thawed and treated with a solution of 50 μg mL^{-1} gentamycin and 1x Halt™ protease/phosphatase inhibitor cocktail (Sigma) for 3 h at room temperature. The samples were then sequentially rinsed twice with decreasing concentrations of water-based solutions: 4 % P/S/G, 2 % P/S/G, and 1 % P/S/G, where P/S is penicillin/streptomycin (Invitrogen #15140–122) and G is gentamycin (VWR #0304). After centrifugation (10k rpm) for 3 min, samples were subjected to 1 % P/S/G and underwent three freeze-thaw cycles, each involving liquid nitrogen exposure for 10 min followed by a 15-min thaw at room temperature. The 1 % P/S/G solution was refreshed between cycles to remove cell debris [25]. Samples were then treated with a red blood cell lysis buffer (eBioscience™, Life Technologies) at room temperature for 45 min. After another freeze-thaw cycle, they were incubated with a cocktail of 2500 U mL^{-1} recombinant DNase I (Millipore Sigma) and 250 U mL^{-1} RNase I (Invitrogen™) in 1 × DNase/RNase buffer at room temperature for 2 h, with agitation at 650 rpm. Finally, after another freeze-thaw step, the extracellular matrix (ECM) samples were submerged in liquid nitrogen for 10 min, lyophilized, and stored at −80 °C.

2.12. Proteomics analyses

2.12.1. ECM protein quantitation and in-solution trypsin digestion

The dried ECM samples were resolubilized with a solution containing 50 mM TEAB pH8.5, 6 M urea, 2 M thiourea, 2 % SDS, 10 mM dithiothreitol (DTT), and 1 × Halt™ proteinase inhibitor cocktail. Protein concentration of each sample was determined by running a precast 10 % Bis-Tris mini-gel with 26-well from Bio-Rad (Hercules) along with a serial amount of *E. coli* lysates (1, 2.5, 5, 10, 15, 20 μg/lane). The SDS gel was visualized with Colloidal Coomassie staining (Invitrogen), imaged by ChemDoc imager, and analyzed by Image Lab 6.1 software (Bio-Rad) for protein quantitation. In-solution digestion was performed on S-Trap micro spin columns (ProtiFi) following a Strap protocol as described previously with slight modification [26,27]. Three micrograms of the protein samples in 44 μL of 50 mM TEAB pH 8.5, 6 M urea, 2 M thiourea, 2 % SDS, 10 mM DTT, 1 × Halt™ were denatured and reduced for 1 h at 34 °C, alkylated with 41 mM iodoacetamide for 1 h in the dark and then quenched with a final concentration of 17 mM DTT. Each sample was digested separately using the S-Trap micro spin column. After quenching, 12 % phosphoric acid was added to a final concentration of 1.2 %. Followed by 1:7 dilution (v/v) with 90 % methanol, 0.1 M TEAB pH 8.5. The samples were then placed into the spin column and centrifuged 4000 *g* for 30 s. Then washed three times with 150 μL 90 % methanol,

0.1 M TEAB pH 8.5. All wash steps were followed by centrifugation at 4000*g* for 30 s. Digestion was performed with 20 μL trypsin at 50 ng μL^{-1} (1:3 w/w) in 50 mM TEAB pH 8.5. The trypsin solution was added to the top of the S-Trap matrix, capped loosely and incubated overnight (16 h) at 37 °C. Following incubation, the digested peptides were eluted off the S-Trap column sequentially with 40 μL each of 50 mM TEAB pH 8.5 followed by 0.2 % formic acid and finally, 50 % acetonitrile. The S-Trap cartridges were centrifuged for 1 min at 4000 *g* following each solvent addition, pooled together and evaporated to dryness by a Speedvac SC110.

2.12.2. Protein identification by nano LC/MS/MS analysis

The tryptic digests were reconstituted in 2 % acetonitrile containing 0.5 % formic acid, and enolase (yeast) tryptic digest was added to each sample with the final concentration of 10 fmol/μL as an internal standard for nanoLC-ESI-MS/MS analysis. The analysis was carried out using an Orbitrap Fusion™ Tribrid™ (Thermo-Fisher Scientific) mass spectrometer equipped with a nanospray Flex Ion Source, and coupled with a Dionex UltiMate 3000 RSLCnano system (Thermo) [26,28]. The peptide samples (10 μL) were injected onto a PepMap C-18 RP viper trapping column (5 μm, 100 μm i. d × 20 mm) at 20 μL min^{-1} flow rate for rapid sample loading and then separated on a PepMap C-18 RP nano column (2 μm, 75 μm × 25 cm) at 35 °C. The tryptic peptides were eluted in a 90 min gradient of 5 %–35 % acetonitrile in 0.1 % formic acid at 300 nL min^{-1}, followed by an 8-min ramping to 90 % acetonitrile-0.1 % formic acid and a 7-min hold at 90 % acetonitrile-0.1 % formic acid. The column was re-equilibrated with 0.1 % formic acid for 25 min prior to the next run. The Orbitrap Fusion was operated in positive ion mode with spray voltage set at 1.6 kV and source temperature at 275 °C. External calibration for Fourier transform, ion trap and quadrupole mass analyzers were performed. In data-dependent acquisition (DDA) analysis, the instrument was operated using FT mass analyzer in MS scan to select precursor ions followed by 3 s "Top Speed" data-dependent CID ion trap MS/MS scans at 1.6 *m/z* quadrupole isolation for precursor peptides with multiple charged ions above a threshold ion count of 10,000 and normalized collision energy of 30 %. MS survey scans at a resolving power of 120,000 (fwhm at *m/z* 200), for the mass range of *m/z* 375–1600. Dynamic exclusion parameters were set at 50 s of exclusion duration with ±10 ppm exclusion mass width. All data were acquired under Xcalibur 4.3 operation software (Thermo-Fisher Scientific).

2.12.3. Data analysis

The DDA raw files for CID MS/MS were subjected to database searches using Proteome Discoverer (PD) 2.5 software (Thermo Fisher Scientific) with the Sequest HT algorithm. The Processing workflow in PD 2.5 contained an additional node of Minora Feature Detector along with a node of "Precursor Ions Quantifier" in the Consensus workflow for precursor ion-based quantification. Both protein identification and protein relatively quantitation analyses among samples within and between the groups were simultaneously achieved. The database search was conducted against a Rattus Norvegicus NCBI database which contains 56,909 sequences plus an additional sequence of yeast enolase. Two-missed trypsin cleavage sites were allowed. The peptide precursor tolerance was set to 10 ppm and fragment ion tolerance was set to 0.6 Da. Variable modification of methionine oxidation, deamidation of asparagines/glutamine; acetylation, M-loss and M-loss + acetylation on protein N-terminus and fixed modification of cysteine carbamidomethylation, were set for the database search. Only high confidence peptides defined by Sequest HT with a 1 % FDR by Percolator were considered for the peptide identification. The final protein IDs contained protein groups that were filtered with at least 2 peptides per protein. Relative quantitation of identified proteins between the two groups was determined by the Label-Free Quantitation (LFQ) workflow in PD 2.5. After retention time alignment for each of the identified peptides across samples, the precursor abundance intensity for each peptide identified by MS/MS in each sample was automatically determined and their unique and razor peptides for each protein in each sample were summed after normalization of yeast enolase abundance and used for calculating the protein abundance by PD 2.5 software.

2.12.4. Bioinformatics analysis

Based on statistical analysis, proteins with fold change >1.2 or <0.833, and $p < 0.05$ were confidently identified as differentially abundant proteins (DAPs) between sample groups and control groups. The heatmap was generated using R studio (https://posit.co, version 2022.07.2 Build 576). Gene Ontology (GO), Kyoto Encyclopedia of Genes and Genomes (KEGG), Reactome Pathways, and protein-protein interaction network analysis for DAPs were performed using STRING (version 11.5, https://string-db.org/).

2.13. Statistics analysis

All data were reported as the mean ± standard deviation (SD). One-way ANOVA statistical analysis was performed to evaluate the significance of the experimental data, followed by Tukey's post hoc test for pairwise comparison. All statistical analyses were executed using Kyplot 2.0 beta 15. When the p-value was less than 0.05, the difference was considered significant. The data were indicated with * for $p < 0.05$, ** for $p < 0.01$, and *** for $p < 0.001$ [29].

3. Results

3.1. Cytocompatibility of M-PAS

The cytocompatibility was accessed by culturing HUVECs on coverslips coated with Cu-PAS. The PLGA served as a control. Cu^{2+} was chosen because among the ions used, Cu^{2+} is a heavy metal and has potential cytotoxicity at high dosage [30]. HUVECs maintained typical endothelial morphology and displayed the same proliferating and spreading behavior on both Cu-PAS and PLGA coatings with few dead cells (Fig. S1, Supplementary Information). MTT assay demonstrated effectively the same metabolic activity on Cu-PAS and PLGA. These results suggested that Cu-PAS was at least as biocompatible as PLGA *in vitro*.

3.2. Graft characterizations

Zn-, Fe-, and Cu-PAS grafts were prepared by adding the Zn-, Fe-, or Cu-PAS solution to the PMMA templates and cured at 150 °C for 6 h. The PAS polymer used in this study had an 11.52 % ligand density of the salicylaldehyde side group (Fig. S2, Supplementary Information), and a weight average molecular weight of 312 kDa (Fig. S3, Supplementary Information). Grafts with a uniform pore structure and a high degree of pore interconnectivity were created using PMMA beads as porogens (Fig. S4, Supplementary Information). Nano-CT showed a highly porous structure of the grafts, with a pore size of 38.61 ± 2.43 μm and porosity of 87.2 ± 0.71 % (Fig. S5, Supplementary Information).

In vitro degradation of the M-PAS grafts showed the impact of changing metal ions on degradation rate (Fig. 1a). Alkaline condition was used to accelerate the degradation of M-PAS. The degradation rate would have been significantly slower if it were conducted in a neutral buffer such as PBS or simulated body fluid under otherwise identical conditions. *In vitro* degradation tests revealed that Zn-PAS degraded the fastest among the three materials. After soaking in 60 mM NaOH solution for 24 h and 48 h, only 27.84 ± 8.54 % and 7.32 ± 5.93 % of the material remained, respectively. Fe-PAS degraded slower than Zn-PAS, with 72.08 ± 9.17 % and 18.42 ± 5.35 % of the material remaining after 24 h and 48 h, respectively. Cu-PAS degraded the slowest, with 81.57 ± 6.49 % and 52.95 ± 7.91 % of the material remaining after 24 h and 48 h, respectively. The most durable Cu-PAS degraded 7.23 times more slowly than the fastest variant Zn-PAS grafts. We think the difference in degradation rate reflects the difference in metal-ligand bond

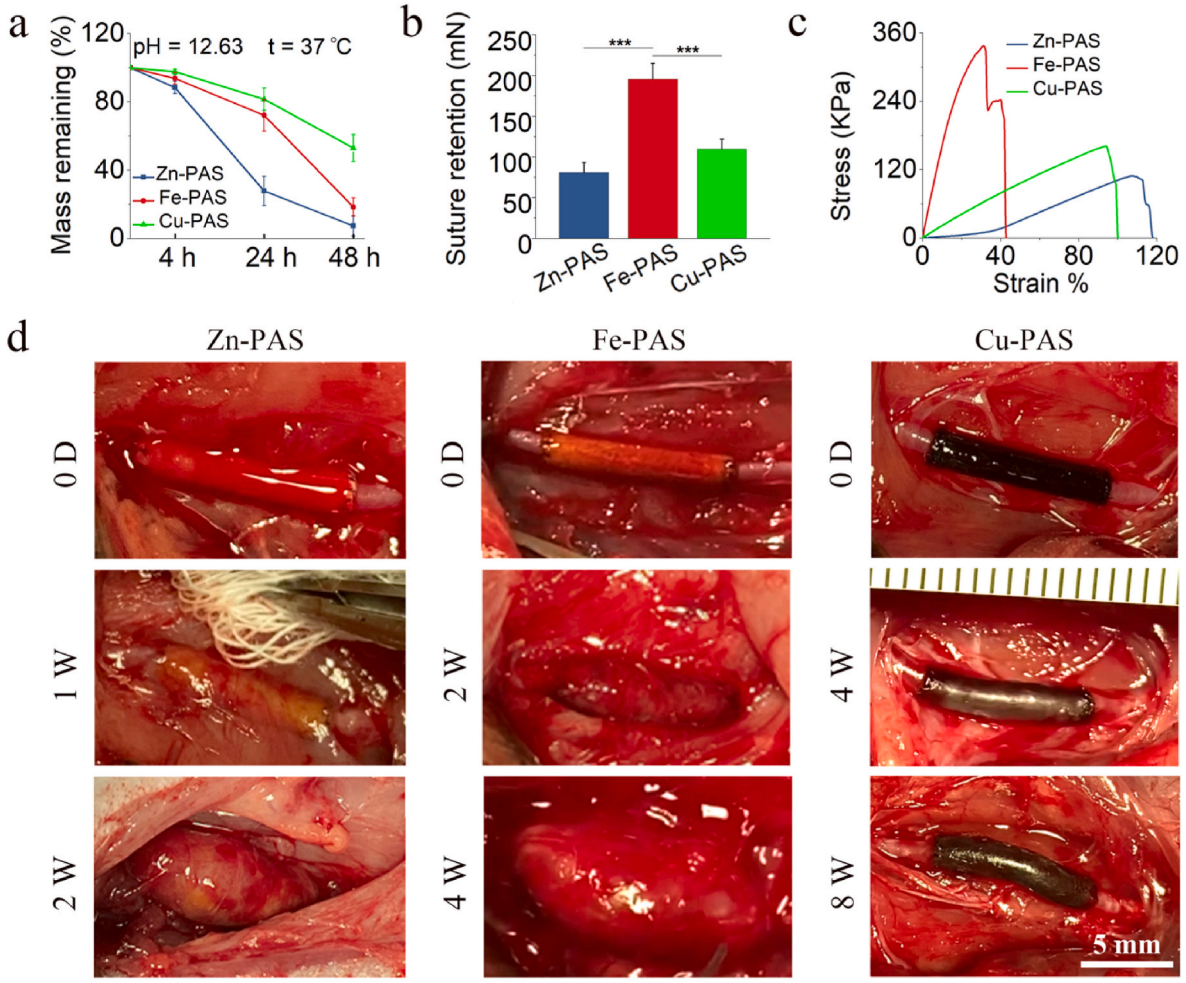

Fig. 1. Comparative evaluation of Zn-, Fe-, and Cu-PAS grafts. (a) *In vitro* degradation. (b) Suture retention forces (mN). (c) Representative stress-strain curves. (d) Gross appearance after interposed into rat carotid arteries for different time intervals. Data in (a) and (b) represent mean ± SD, N = 3. Significant difference: ***, $p < 0.001$.

strength, which play a critical role in the overall network stability and degradation behavior of the materials. Zn-Schiff base bonds are weaker than that of Cu-Schiff base. While Fe forms strong bonds with Schiff base, it prefers to bind 6 ligands. Therefore, Fe would need 3 PAS side chains to satisfy its preference for a hexagonal ligand arrangement. This is harder to achieve than Cu that prefers to bind 4 ligands, thus only needs to bring 2 PAS side chains to close proximity for binding. We believe this contributes to the weak Fe-PAS crosslink and consequently faster degradation.

Suture retention force of the three types of grafts were compared (Fig. 1b). Fe-PAS showed the highest suture retention (195.53 ± 19.41 mN). Zn-PAS showed the lowest suture retention (80.90 ± 12.12 mN). Nevertheless, the Zn-PAS grafts could still be sutured in the rat carotid models. Tensile tests revealed stress-strain curve characteristics of the M-PAS grafts with varied mechanical strength and stretchability (Fig. 1c, Fig. S6, Supplementary Information). By alternating the metal ions, we can change the mechanical properties of the grafts [31]. Fe-PAS grafts were the toughest, with a UTS of 462.10 ± 94.72 kPa, a strain of break at 38.75 ± 7.10 %, and modulus of 1120.87 ± 214.35 kPa; Zn-PAS grafts were the softest, with a UTS of 101.02 ± 15.07 kPa, a strain of break at 95.40 ± 9.17 %, and modulus of 37.92 ± 12.30 kPa; Cu-PAS grafts had medium toughness: with a UTS of 166.44 ± 8.28 kPa, a strain of break at 103.74 ± 17.01 %, and modulus of 184.70 ± 49.76 kPa.

Our goal in the first phase of the study was to determine which metal ions would be appropriate for vascular graft fabrication. We evaluated the early-stage performance of Zn-, Fe-, and Cu-PAS grafts using a rat carotid artery interposition model (Fig. 1d). Within the first week, Zn-PAS grafts seemed promising. However, by the second week, they began to show pronounced dilation, hinting at an overly fast degradation or insufficient mechanical strength to sustain the artery's repeated pulsations (Fig. S7a, Supplementary Information). Subsequently, we assessed the Fe-PAS grafts. Fe-PAS grafts have a better elasticity [21] and slower degradation (Fig. 1a) compared to Zn-PAS grafts. Though the Fe-PAS grafts did exhibit reduced dilation by the end of the second week, significant dilation was still observed by the fourth week (Fig. S7b, Supplementary Information). Among all grafts tested, the Cu-PAS grafts degraded most slowly, remained patent and exhibited negligible dilation after 8 weeks (Fig. 1d). The unsatisfactory outcomes with Zn-PAS and Fe-PAS grafts are likely caused by misalignment in degradation and host ECM deposition as revealed by the benchtop testing on degradation and mechanical properties. Thus, based on these initial *in vivo* evaluations, Cu-PAS was identified as the most suitable graft material and was the focus for the rest of the study.

SEM images revealed that Cu-PAS grafts exhibited a uniform distribution of pores across the ablumen, lumen, and wall, with no discernible skin layers on their surfaces (Fig. 2a). The wall thickness of the Cu-PAS grafts was 245.48 ± 24.86 μm. Cu-PAS grafts were soft, elastic, and had good handling characteristics. Upon removal of the external forces, the grafts recovered to the original shape after either compression or expansion by tweezers multiple times (Fig. 2b–Supplementary Video 1 and 2). A 5-cm long Cu-PAS graft was prepared (Fig. S8, Supplementary

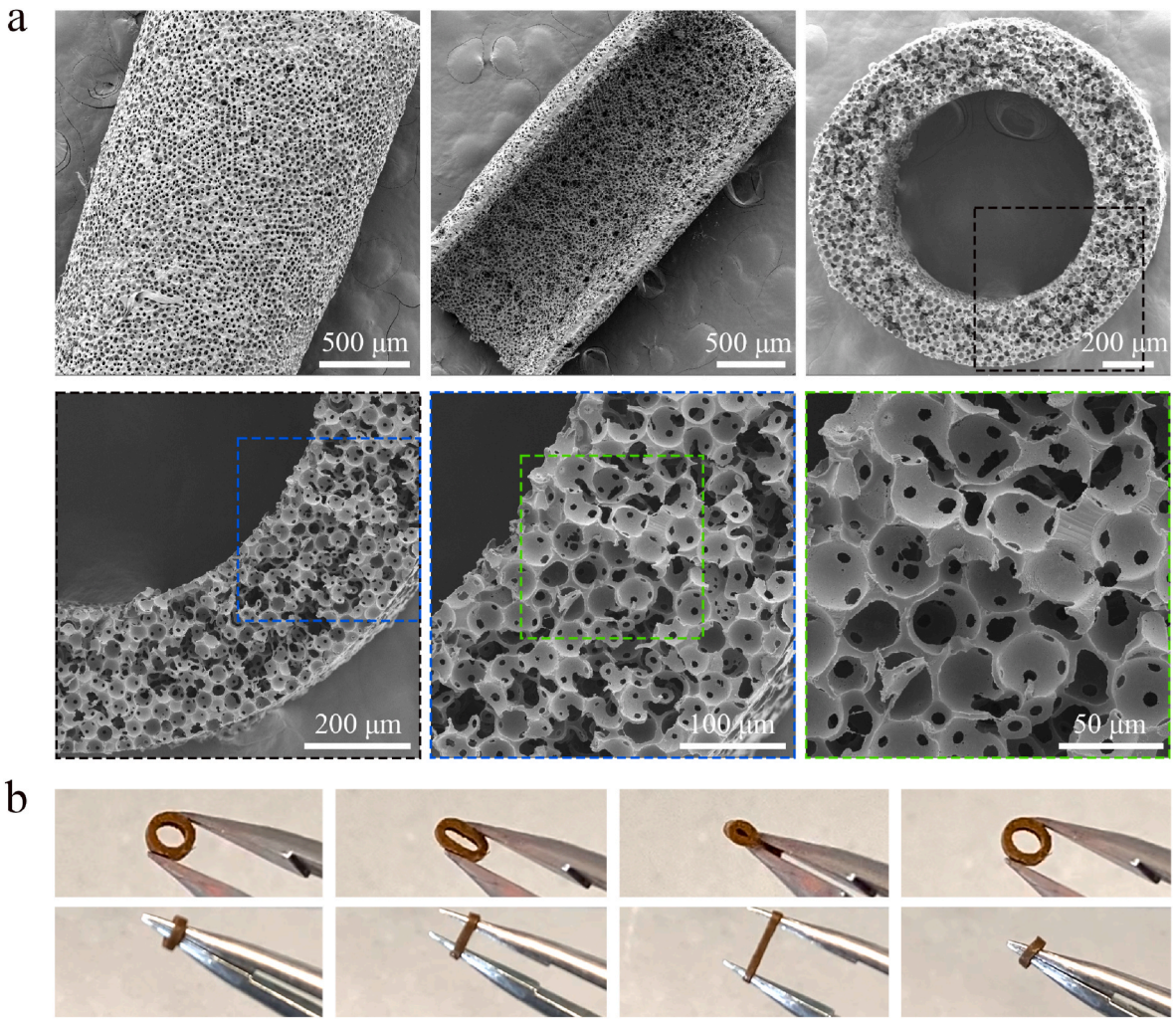

Fig. 2. Pore structure and handling experience of Cu-PAS grafts. (a) SEM image of the ablumen, lumen, and cross-sections at low and high magnifications. (b) Images depicting the Cu-PAS grafts retaining their initial shape after external forces from tweezers were released.

Information). Tapping one end of the graft sent a mechanical wave across its length, leading to dynamic deformation. This transformation in shape-shifted the light reflection on the graft, producing a shifting shadow (Supplementary Video 3). The 5-cm Cu-PAS graft could be elongated to approximately 180 % without breaking or rupture and recoiled to its original length (Fig. S8, Supplementary Information; Supplementary Video 3), demonstrating good elasticity and toughness of the Cu-PAS grafts.

3.3. Graft implantation and patency

Cu-PAS grafts were interposed in the left common carotid artery of 26 Sprague Dawley rats, while the contralateral carotid artery served as a control. 96 % of the animals survived >24 h after the implantation (Fig. S9a, Supplementary Information). Perioperative mortality of 1 rat was attributed to bleeding near the anastomoses; autopsies revealed an intact graft with hemorrhages near the surgical site. This graft was excluded as an outlier. It was likely a surgical error or a significant graft manufacturing defect that set it apart from the rest of the grafts. This reduced the total sample size to 25 rats. One animal died on day 225 at the age of 17 months, exhibiting no complications. The graft was intact and patent. One rat died on day 32 due to graft rupture. Occlusions were noted in a total of 5 animals, three on day 28, one each on day 90 and day 296 (Fig. S9b, Supplementary Information). The overall patency rate was 76 %, calculated by formula (25-6)/25 = 76 %. Fig. 3a shows the macroscopic views of the Cu-PAS grafts at various time intervals. Initially, the grafts exhibited a distinct dark green color because of the presence of copper, a clear distinguishing feature from the native artery. This color gradually lightened over the course of the study. Starting at 8 months, the walls of the grafts became more translucent resembling the appearance of an artery. Noticeably, a confluent neointima was present within the grafts starting from 4 months and continuing through 8 and 12 months (Fig. 3c; Fig. S10, Supplementary Information).

Ultrasound examinations conducted at 4 days, 1 month, 4 months, 8 months, and 12 months after implantation showed that the grafts had an open lumen and adequate blood flow, akin to that of the native carotid artery. On day 4, backflow(visually represented as red color) was observed at the site of anastomosis, signifying turbulence in the blood flow. However, this backflow was significantly reduced by 1-month (Fig. 3b). The grafts maintained a steady and smooth lumen with no significant distortion at all time points. We determined the graft size using an average of several measurements of rat carotid artery before initiating the implantation. The artery of the rats receiving the implants was smaller, as the ultrasound at 4-day postimplantation revealed that the graft was 19.1 % larger than the contralateral artery (Fig. 3d). We don't believe this is dilation because Cu-PAS is highly elastic, and neither Cu-PAS nor PCL would have degraded appreciably at day 4. Instead, this 19.1 % increase likely reflects an issue with the initial oversized design of the grafts. The grafts dilated by 24.9 % at 8 months and 27.6 % at 12 months when compared to contralateral arteries.

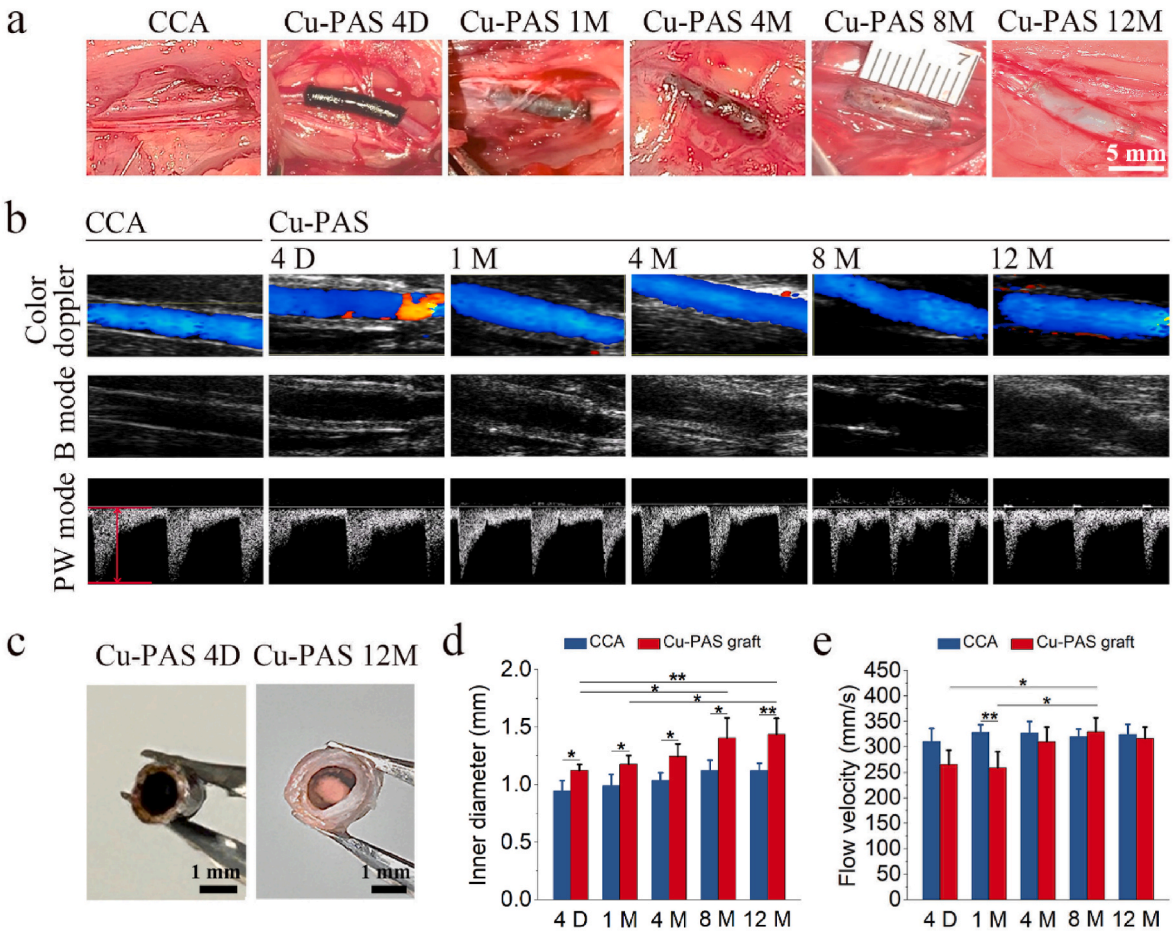

Fig. 3. Graft implantation and patency. (a) Gross appearance of the Cu-PAS graft explants after interposed into the rat left carotid arteries for 4 days, 1 month, 4 months, 8 months, and 12 months. (b) Representative ultrasound images of the common carotid artery (CCA) and Cu-PAS grafts. Top row: color Doppler mode; Middle row: brightness (B) mode; Bottom row: pulse wave (PW) mode. (c) Gross transverse view of the Cu-PAS graft explants post-implantation for 4 days and 12 months. (d) Inner diameter measured by B-mode images. (e) Flow velocity measured in the middle region of the grafts and native carotids by PW mode images. Data in (d) and (e) represent mean ± SD, N = 4. Significant difference: *, $p < 0.05$; **, $p < 0.01$; ***, $p < 0.001$. (For interpretation of the references to color in this figure legend, the reader is referred to the Web version of this article.)

Taking into account the initial oversized design, the actual dilation of the grafts ranged from 5.8 % to 8.5 %. Notably, there was no significant change in the inner diameter of the grafts between the 8-month and 12-month evaluations, suggesting that the dilation had stabilized (Fig. 3, b and d).

Quantification of the flow rate, represented by the distance between two parallel red lines in the pulsed-wave images, revealed a post-implantation decrease in the grafts' flow rate at day 4 and 1 month. The flow rate reverted to the native arteries' level by the fourth month. The uniformity of the inner diameters and flow rates indicated that the Cu-PAS grafts provided a stable mechanical support through the host modification process. This reflected a balance between the degradation of the graft and the deposition of host vascular tissue (Fig. 3b–and e).

3.4. Histological and morphological assessments

Histological examination of graft explants initially focused on the transverse cross-sections from the middle region of the Cu-PAS grafts (Fig. S11, Supplementary Information; Fig. 4a). The grafts showed consistent morphological changes without signs of stenosis. By 4 days, cells infiltrated entire grafts. By 1 month, the graft material showed signs of degradation, with collagen fibers forming at the ablumen. At 4 months, the lumen had fully endothelialized, and a cellularized neo-intima had formed. By 8 months, only around 20 % of the Cu-PAS polymer remained. The wall exhibited circumferentially organized cells and extracellular matrix, with a distinct media-like layer. By 12 months, the host remodeled the graft into a neoartery, as evidenced by approximate 90 % degradation of the Cu-PAS, and changes in morphology and cell density in the grafts, despite having a thicker wall and a larger lumen.

To enhance the detectability of the Cu-PAS polymer residue within the grafts as they remodeled over time, we inspected unstained slides from various time intervals under red fluorescence (Cy5 filter, Fig. S12, Supplementary Information). The Cu-PAS polymer residues appeared brighter under fluorescence microscopy than the regenerated tissue. This increased brightness was due to light scattering caused by the polymer residue's distinct optical properties compared to the surrounding tissue. The quantification of the Cu-PAS residue (%) revealed the progression of graft degradation (Fig. S12b, Supplementary Information). Compared to day 4 grafts, 19.99 ± 6.67 % and 5.87 ± 2.93 % of the materials remained at 8 months and 12 months, respectively.

We conducted a histological examination of the longitudinal cross-sections that spanned half the length of the explanted grafts (Fig. S11, Supplementary Information; Fig. 4b). By 4 months, a confluent neo-intima was present in the lumen of the grafts. From proximal to the middle of the grafts, consistent luminal area and wall thickness were observed at all time points, with no signs of stenosis. The grafts demonstrated durability; although dilation was observed, there were no indications of aneurysm formation. Morphometrical analysis revealed that the luminal area of the Cu-PAS grafts increased gradually in the first

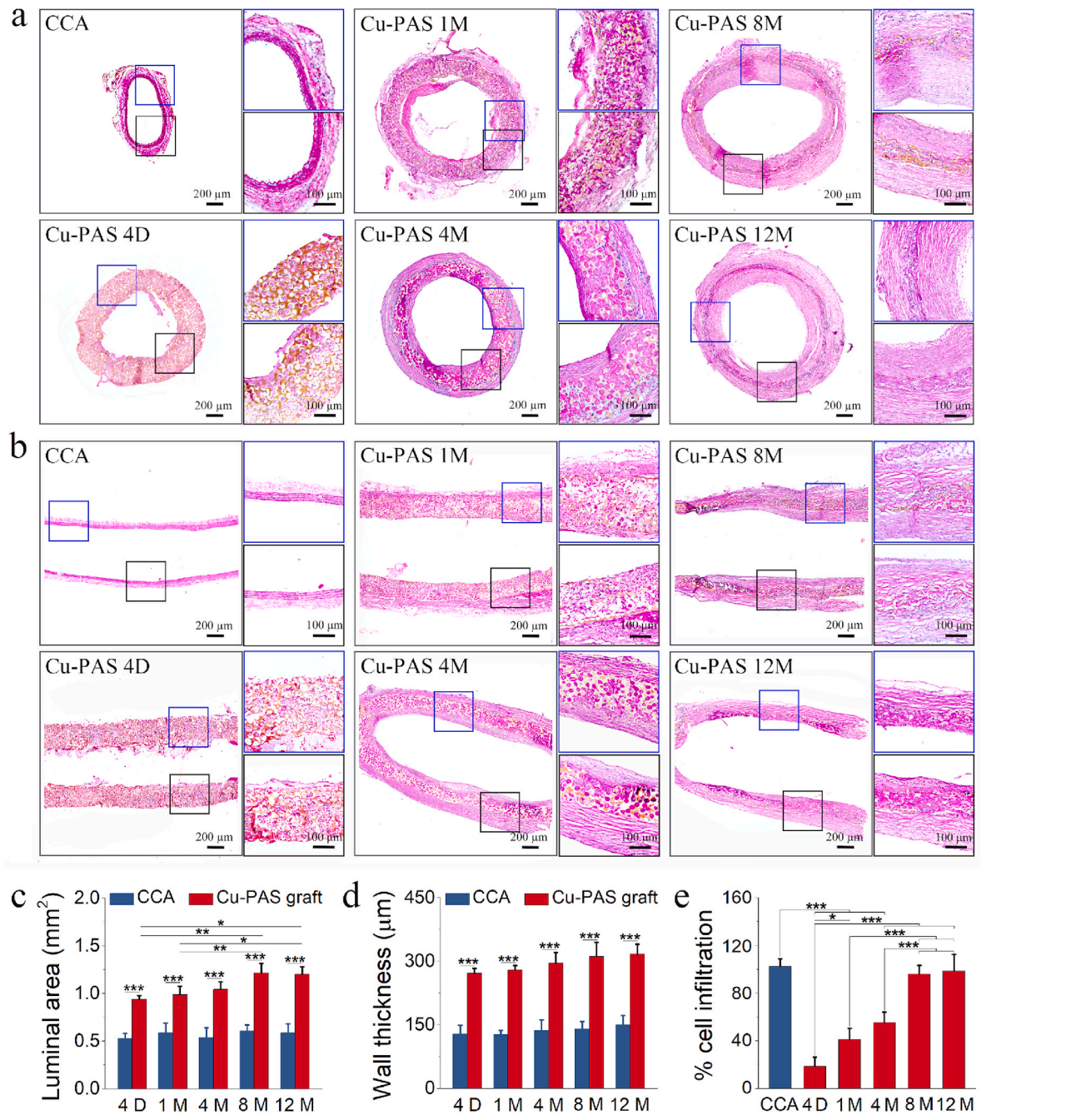

Fig. 4. Histological evaluations and morphological measurements. (a) Cross-sectional H&E-stained images of the central region of Cu-PAS grafts at intervals of 4 days, 1 month, 4 months, 8 months, and 12 months after implantation. (b) H&E-stained longitudinal sections of Cu-PAS grafts at intervals of 4 days, 1 month, 4 months, 8 months, and 12 months after implantation. (c) Luminal area (mm^2). (d) Wall thickness (μm). (e) Cell infiltration (%). Measurements for (c), (d), and (e) were based on H&E-stained cross-sections of four independent samples. Scale bars in (a) and (b), 200 μm (left column) and 100 μm (right column). Data in (c), (d), and (e) represent mean ± SD, N = 4. Significant difference: *, $p < 0.05$; **, $p < 0.01$; ***, $p < 0.001$.

8 months, stabilizing between 8 and 12 months. The grafts had significantly larger luminal areas and wall thickness than contralateral native carotids at all time points ($P < 0.001$, Fig. 4c–and d).

The porous structure of the Cu-PAS grafts facilitated rapid cell infiltration (Fig. 4e; Fig. S13, Supplementary Information). During the initial 4 months, cellular infiltration was prominent from the adventitial side towards the graft matrix. This infiltration was mainly composed of macrophages and fibroblasts. At 8 months, the cellular population was comparable to that of the native artery and stabilized. By 12 months, the entire grafts were repopulated with cells and remodeled into living neoartery.

3.5. Inflammatory responses

CD68 staining was used to visualize the presence and distribution of macrophages in the Cu-PAS grafts (Fig. 5). The $CD68^+$ cell ratio decreased substantially at 8 and 12 months compared to 1 and 4 months, correlating with graft degradation. At 1 and 4 months, $CD68^+$ cells were distributed throughout the grafts, while at 8 months, they were only present in regions where residue of the Cu-PAS polymers remained, and in the. By 12 months, $CD68^+$ cells were absent in the regions where the Cu-PAS material had completely degraded (Fig. 5 a and d). Both CD206 and iNOS were observed at all time points (Fig. 5 b, c, e, and f). At 1 and

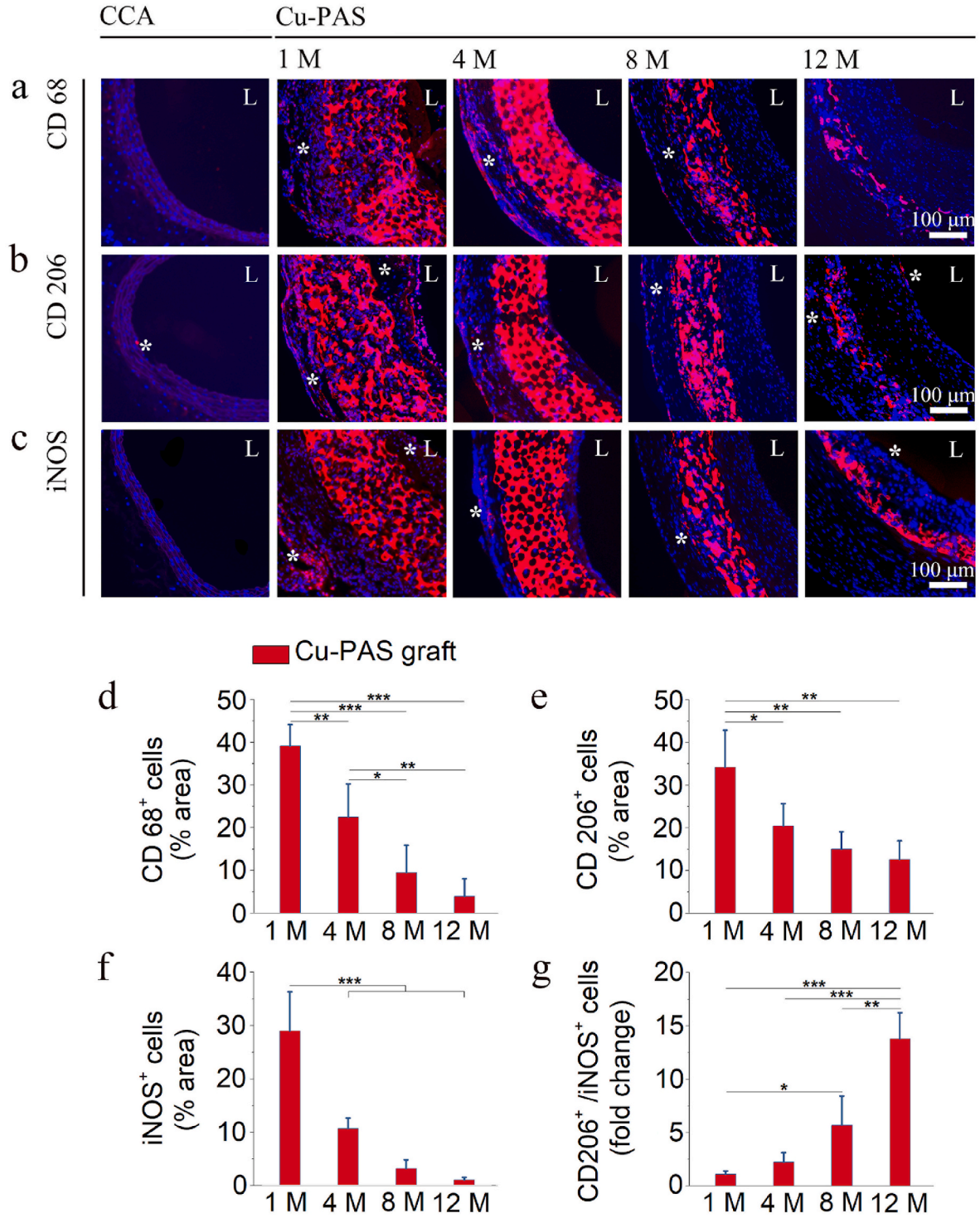

Fig. 5. Macrophage infiltration and polarization. (a) Representative images for immunofluorescence staining with the pan-macrophage marker CD68. Positive staining is indicated with asterisks *. (b) Images showcasing immunofluorescence staining with the M2 macrophage marker CD206. Positive staining is indicated with asterisks *. (c) Images for immunofluorescence staining with the M1 macrophage marker iNOS. Positive staining is indicated with asterisks *. (d) Percentage of $CD68^+$ cells in grafts (e) Percentage of $CD206^+$ cells in grafts. (f) Percentage of $iNOS^+$ cells in grafts. (g) The ratio of $CD206^+$ cells/$iNOS^+$ cells in grafts. Blue colors in (a)–(c) indicate the nucleus and red indicates positive staining. L indicates lumen. Data in (d)–(g) represent mean ± SD, N = 4. Significant difference: *, $p < 0.05$; **, $p < 0.01$; ***, $p < 0.001$. (For interpretation of the references to color in this figure legend, the reader is referred to the Web version of this article.)

4 months, CD206 and iNOS expression levels were high. By 8 months, CD206 remained relatively high, while iNOS levels decreased. At 12 months, numerous $CD206^+$ cells but few $iNOS^+$ cells were observed within the grafts. The M2/M1 ratio, an indicator of remodeling, was calculated based on the corresponding CD206 and iNOS expression levels. The data showed a significant increase in the M2/M1 ratio after 4 months (Fig. 5g), which remained at a high level for 8 and 12 months, indicating the remodeling of the grafts was ongoing. Of note, all Cu-PAS material residue areas were excluded to reduce false positives because of light scattering caused by the polymer before quantifying the area of

cells that were positively stained and the area positive for DAPI staining (Fig. S14, Supplementary Information).

3.6. Endothelial cell coverage and smooth muscle cell distribution

A thin layer of endothelium was observed on the lumen of the grafts at 1 month, which was maintained to the last data point at 12 months (Fig. 6a). Additionally, SEM of the graft lumen explanted at 12 months (Fig. S15, Supplementary Information) revealed a distinct layer of ECs completely covering the lumen. The ECs were aligned in the direction of the flow, resembling that of native carotids. CD31 en face imaging revealed tightly bound ECs with a cobblestone-like morphology, similar to those found in the native artery (Fig. 6b and c). CD31 IHC staining of 12-month explant cross-sections revealed brown-stained thin layers on the luminal surface of carotid arteries and grafts, further indicating endothelialization of the lumen(Fig. S16, Supplementary Information).

The calponin^{+} and αSMA^{+} staining revealed smooth muscle cells (SMCs) distributed in the wall of the grafts (Fig. 6d). At 1 month, the SMCs were dispersed throughout the graft wall. Starting from 4 months, the remodeled grafts showed a dense, concentric SMC layer, resembling the media layer of native arteries.

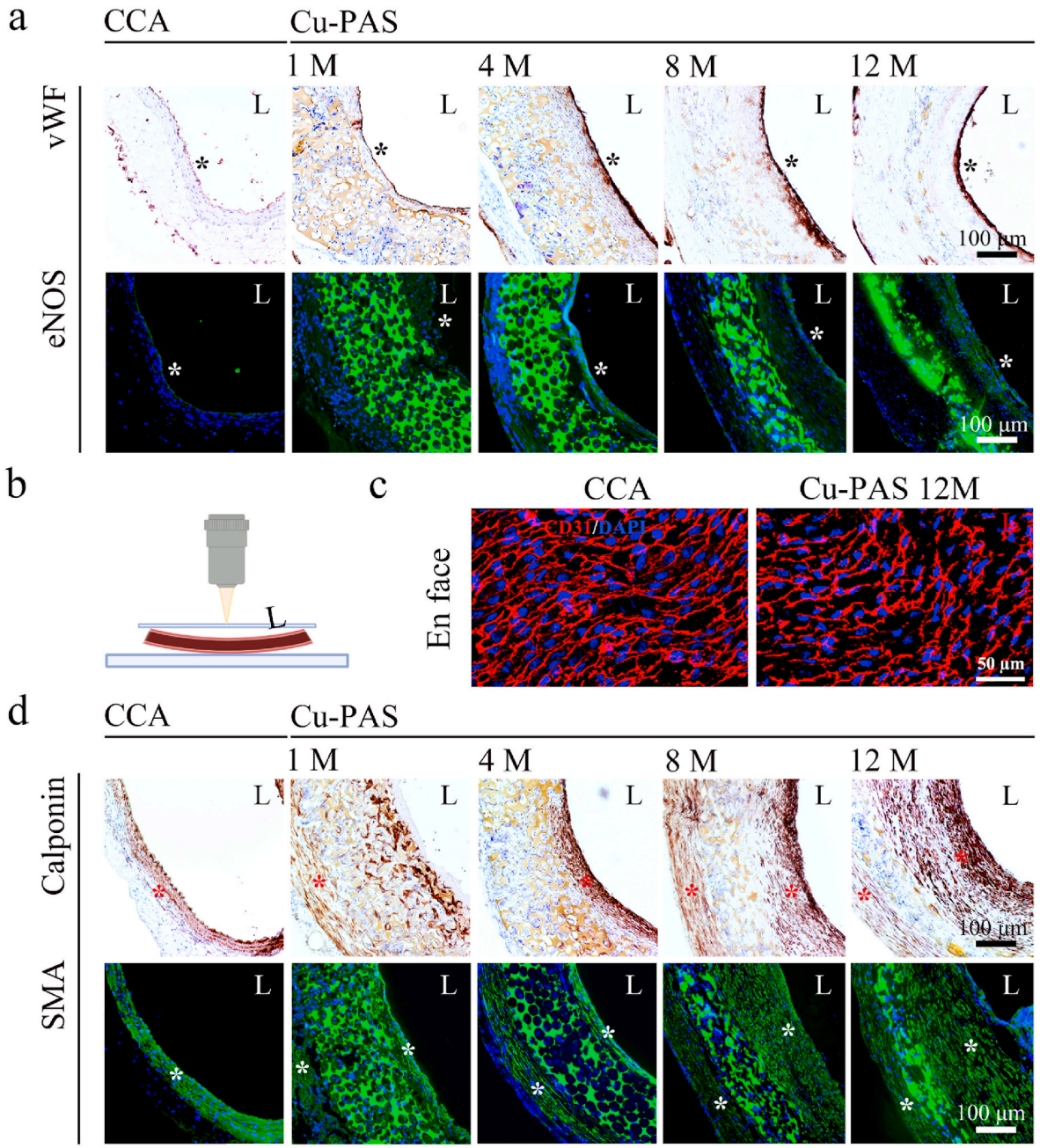

Fig. 6. Endothelium coverage and smooth muscle cell distribution. (a) Immunohistochemical staining of vWF and immunofluorescence staining of eNOS in Cu-PAS graft explants, post-interposition in rat left carotid arteries at 4 days, 1 month, 4 months, 8 months, and 12 months. (b) Schematic depicting the positioning of samples for the observation of the endothelial layer using multiphoton microscopy. (c) Representative images for en-face immunofluorescence staining with EC markers, CD31. Scale bar, 100 μm. (d) Immunohistochemical staining of calponin and immunofluorescence staining of SMA. Blue colors indicate the nucleus, and brown, green, or red colors indicate positive staining (marked with asterisks *). L indicates lumen. (For interpretation of the references to color in this figure legend, the reader is referred to the Web version of this article.)

3.7. ECM protein distribution

Cu-PAS grafts at all time points showed no signs of calcification based on ARS staining (Fig. S17, Supplementary Information). Histological analysis revealed circumferentially organized collagen fibers spanning the wall and elastic fibers near the lumen after 4 months, which remained organized and similar to native carotids for 12 months (Fig. 7a). Expression of collagen I was observed mainly in the adventitia and media layers of the grafts (Fig. 7b). Col III was distributed in the same regions but at a lower level. Picro-Sirius red staining highlighted the collagen networks in the grafts, which were initially separated by the Cu-PAS polymer that had not yet degraded at 4 months and then fully connected in the walls of the 8-month and 12-month remodeled grafts (Fig. 7b). Under multiphoton microscopy, en face imaging of elastin in the lumen (Fig. S18, Supplementary Information) and collagen fibers on the ablumen (Fig. S19, Supplementary Information) of the 12-explants were visualized. The fiber orientations and thickness were similar to those of native carotids.

3.8. Mechanical properties

Fully transformed 12-month explants displayed a compliant nature, with a circumferential pressure-strain curve that was similar to that of native arteries, albeit with a smaller toe region (Fig. 7c). The circumferential stretch of the grafts increased with an increase in pressure from 0 to 92 mmHg. The change in circumferential stretch was more limited when the pressure was above 92 mmHg. There was no significant difference in the burst pressure, a marker of bulk strength, between the remodeled 12-month grafts and the native artery (Fig. 7e). The remodeled 12-month grafts were less compliant than native arteries ($P < 0.05$, Fig. 7d).

3.9. Proteomics analysis

3.9.1. Overview of the proteome information

Proteomics analysis was performed for 12-month grafts. In the decellularized ECM of the 12-month remodeled grafts, we identified over 700 proteins through quantitative proteomics analysis (Detailed data in All Proteins spreadsheet, Supplementary Information 2), with a wide molecular weight range spanning from 11.1 to 863.7 kDa. The ECM from these grafts encompassed crucial components that closely resembled those found in the native carotid artery. These components endowed the remodeled grafts with structural integrity, elasticity, and support essential for arterial functions. Key components included fibrillar collagens such as collagen types I, III, and V, elastin, proteoglycans like versican and lumican, glycoproteins including laminin and vWF, as well as integrins, fibulins (including fibulin-1 precursor), and fibrillins. Collectively, these proteins contribute to ECM organization, cell adhesion, and tissue structure. Of all the proteins discovered, a statistical analysis identified 98 differentially abundant proteins (DAPs) based on fold change criteria (fold change >1.2 or < 0.833) and significance ($p < 0.05$). These DAPs included 57 proteins with increased abundance and 41 with decreased abundance. Hierarchical clustering analysis of these proteins yielded a heatmap (generated using R studio https://posit.co, version 2022.07.2 Build 576) illustrating protein profiles across the 12-month Cu-PAS grafts and native carotids (Fig. S20, Supplementary Information).

3.9.2. Bioinformatics analysis of DAPs

3.9.2.1. Protein-proteins interaction analysis. The protein-protein interaction network was analyzed using the publicly available program STRING and the results are shown in Fig. 8a and b. The main upregulated proteins, such as thrombospondins (Thbs4, Thbs1, Thbs2), secreted phosphoprotein 1 (Spp1), integrin subunit alpha 1 (Itga1), vitronectin (Vtn), desmin (Des), alpha-2-HS-glycoprotein (Ahsg), tenascin C (Tnc), collagen type XII alpha 1 (Col12a1), matrix metallopeptidase 12 (Mmp12), apolipoprotein E (Apoe) and matrix gla protein (Mgp), were involved in multiple pathways. Several important pathways were cell adhesion/migration/signaling, focal adhesion, PI3K-Akt signaling pathway, angiogenesis modulation, tissue remodeling, inhibition of vascular calcification, extracellular matrix degradation/organization, lipid metabolism and vascular repair, which are all relevant to neoartery regeneration or vascular biology in general. The main decreased abundance proteins, such as Col4a5, Col4a6, and Col15a1, Integrin alpha 2b (Itga2b), integrin beta 3 (Itgb3), Laminin alpha 2 (Lama2) and Laminin beta 1 (Lamb1), vWF, were involved in multiple pathways including downregulating the structural integrity and extracellular matrix composition of the neoartery, thrombotic events, and endothelial cell behaviors, which may be related to the anti-thrombosis events and maturation of the regenerated neoartery.

3.9.2.2. Gene ontology (GO) functional analysis. Functional classification of the 57 upregulated and 41 downregulated DAPs involved GO analysis, encompassing biological processes (BP), cellular components (CC), and molecular functions (MF). In the BP subcategory, the major upregulated DAPs were involved in tissue development, system development, anatomical structure development, developmental process, cell adhesion, regulation of cellular component movement, anatomical structure morphogenesis, regulation of cell migration, cellular component organization or biogenesis, cell differentiation, cytoskeleton organization, and regulation of developmental process (Fig. 8c). The major decreased abundance DAPs were involved in cell adhesion, cellular response to chemical stimulus, cellular response to organic substance, and cellular component organization (Fig. S21a, Supplementary Information). In the CC subcategory, major increased abundance DAPs were involved in extracellular matrix, collagen-containing extracellular matrix, supramolecular fiber, extracellular region, polymeric cytoskeletal fiber, cytoskeleton, actin cytoskeleton, and intracellular non-membrane-bounded organelle (Fig. 8d); The major DAPs with decreased abundance were involved in collagen-containing extracellular matrix, extracellular matrix, extracellular region, extracellular space and cell junction (Fig. S21b, Supplementary Information). In the MF subcategory, major DAPs with increased abundance were involved in protein-containing complex binding, glycosaminoglycan binding, cell adhesion molecule binding, and structural molecule activity (Fig. 8e); The major decreased DAPs were involved in extracellular matrix, basement membrane, and extracellular region (Fig. S21c, Supplementary Information).

The enrichment of pathways, as indicated by GO terms associated with DAPs, are closely related to the various cellular and molecular processes involved in neoartery regeneration. These processes include cell adhesion, cytoskeleton organization, tissue morphogenesis, and regulation of cell migration, among others. The proper coordination of these pathways is crucial for successful neoartery regeneration and the establishment of functional arterial structures.

3.9.2.3. Reactome pathway analysis. Reactome pathway analysis for the DAPs showed that the significantly enriched pathways included smooth muscle contraction, extracellular matrix organization, ECM proteoglycans, degradation of the extracellular matrix, and integrin cell surface interactions (Fig. 8f). The downregulated pathways included extracellular matrix organization, elastic fiber formation, and hemostasis (Fig. S21d, Supplementary Information). Overall, these pathways play crucial roles in various aspects of the neoartery regeneration and maturation process. They help in tissue remodeling, cell-matrix interactions, cell proliferation and migration, and the establishment of a functional and properly structured neoartery capable of supporting blood flow and physiological functions.

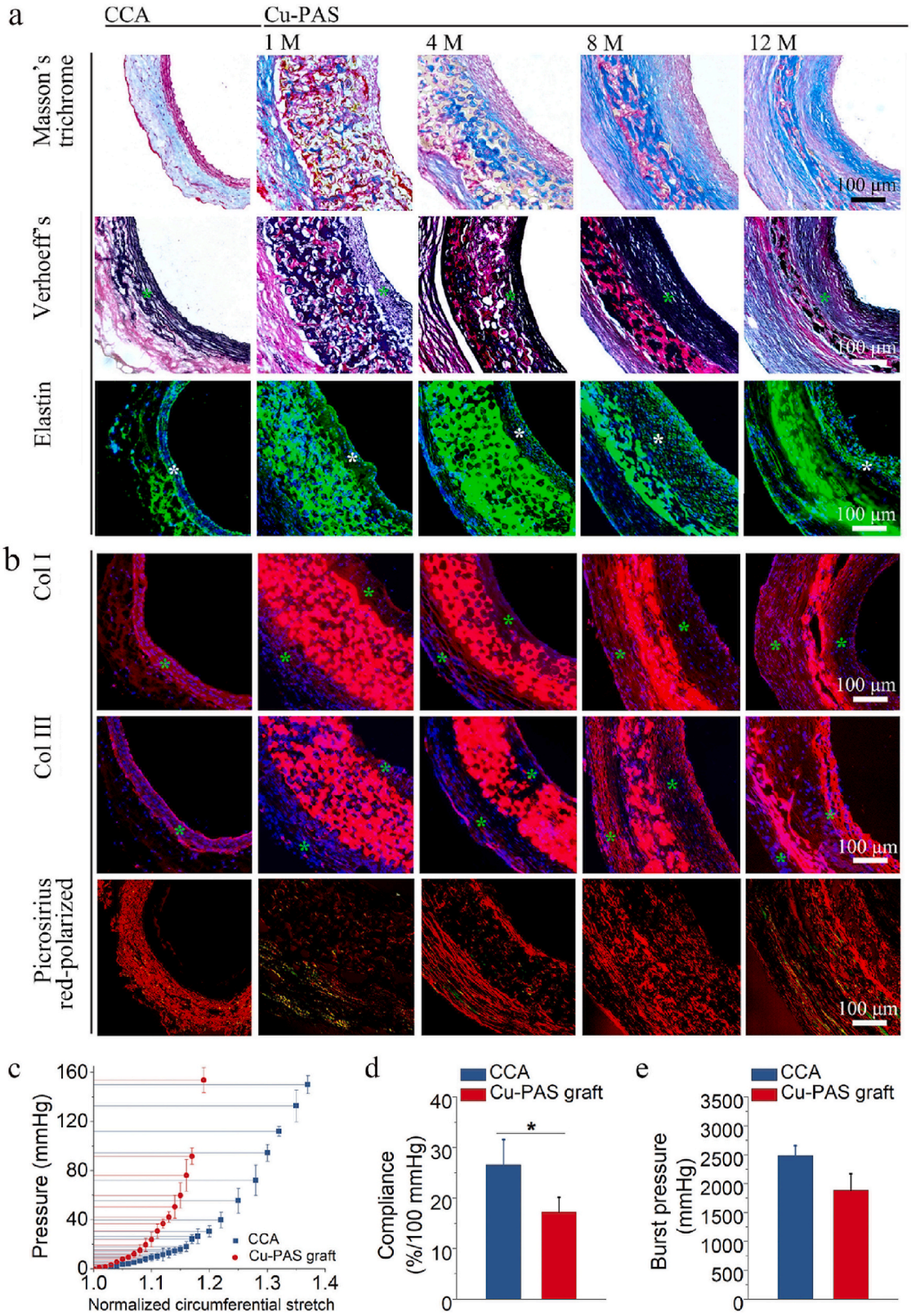

Fig. 7. ECM protein deposition and mechanical assessment. (a) Histochemical staining of Masson's trichrome, Verhoeff elastin, and immunofluorescence staining of elastin after grafts being interposed into rat carotid arteries for 4 days, 1 month, 4 months, 8 months, and 12 months. Collagen in Masson's trichrome staining: blue; Elastin in Verhoeff's elastin and immunofluorescence staining: black and green (marked with asterisks *). (b) Immunofluorescence staining of collagen I, collagen III, and histochemical staining of Picrosirius red. Blue colors indicate the nucleus and red colors indicate positive staining (marked with asterisks *). (c) Circumferential pressure-stretch curves of grafts explanted after 12 months. (d) Compliance of grafts explanted after 12 months. (e) Burst pressure of grafts explanted after 12 months. Data represent mean ± SD, N = 3. Significant difference: *, $p < 0.05$. (For interpretation of the references to color in this figure legend, the reader is referred to the Web version of this article.)

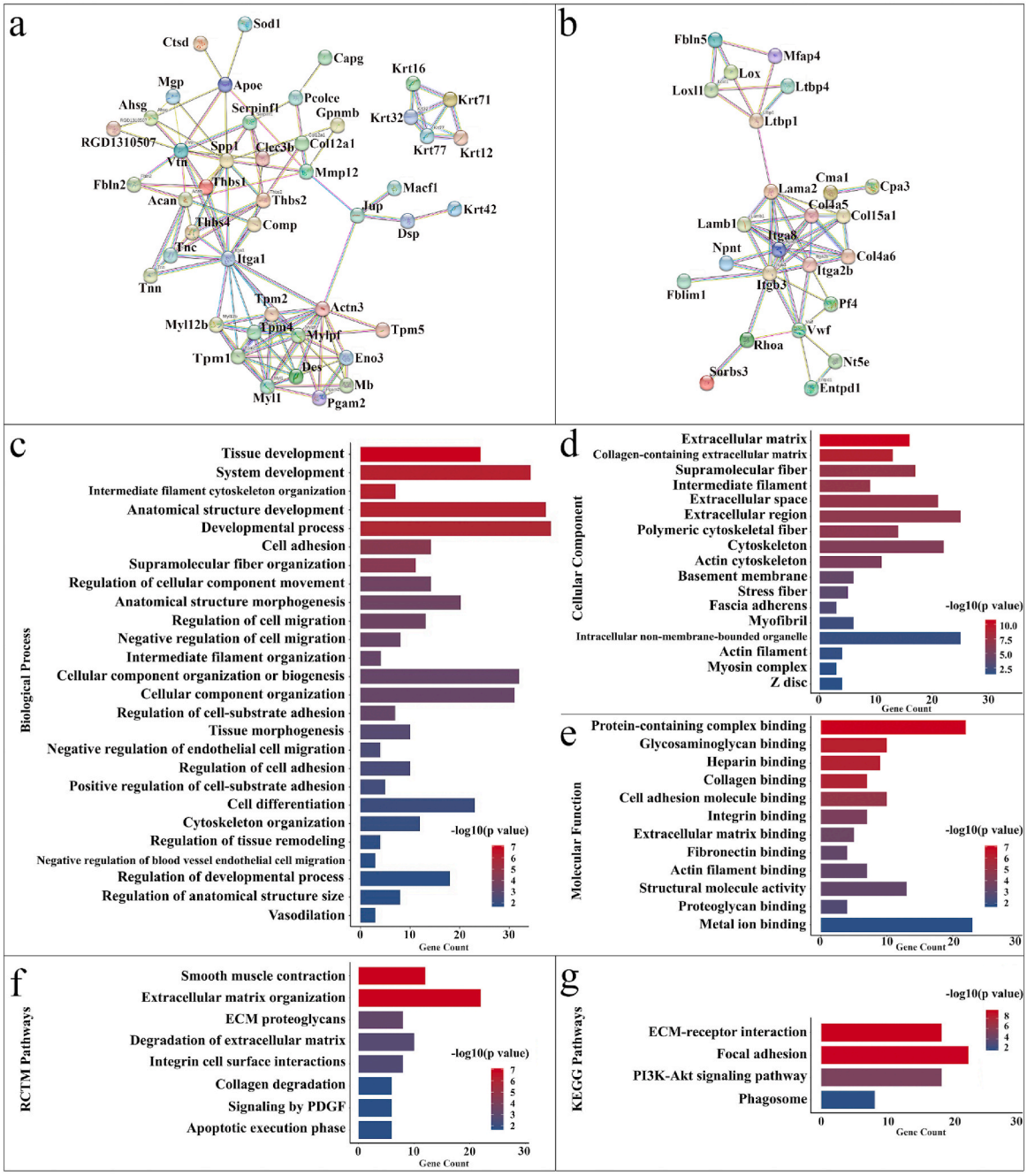

Fig. 8. Proteomics analysis in 12-month Cu-PAS graft explants. (a) Protein-protein interaction network of upregulated DAPs analyzed by STRING software. Each note represents a protein and lines represent interactions. (b) Protein-protein interaction network of downregulated DAPs. (c) Gene Ontology (GO) enrichment analysis for biological processes (BP), (d) GO enrichment for cellular components (CC), (e) GO enrichment for molecular functions; (f) Pathways enriched according to Reactome (RCTM) classification of DAPs; (g) Pathways enriched based on KEGG classification of DAPs. The y-axis represented the significantly upregulated pathways, while the x-axis showed the count of proteins for each category. DAPs: differentially expressed proteins. Different colors indicated different P-valves. (For interpretation of the references to color in this figure legend, the reader is referred to the Web version of this article.)

3.9.2.4. Kyoto Encyclopedia of Genes and Genomes (KEGG) biological pathway analysis. KEGG pathway analysis for the DAPs showed that the significantly enriched pathways include ECM-receptor interaction, focal adhesion, PI3K-Akt signaling pathway, and phagosome (Fig. 8g). The downregulated pathways included ECM-receptor interaction, focal adhesion, PI3K-Akt signaling pathway and protein digestion and absorption (Fig. S21e, Supplementary Information). Overall, these pathways were likely involved in orchestrating various cellular processes critical for neoartery regeneration and maturation. They play roles in cell-matrix interactions, cell proliferation and migration, tissue remodeling, and proper contractility of SMCs within the arterial wall. Proper coordination of these pathways is essential for the successful regeneration, maturation and functional restoration of the artery.

4. Discussion

Developing vascular grafts that mimic the biomechanical and physiological traits of natural blood vessels remains a challenge [32]. There's growing interest in resorbable grafts, which are gradually replaced by new vascular tissues, but achieving the right balance between material

degradation and tissue regeneration is critical [33,34]. As to materials, issues with degradation rates, mechanical strength, cellular integration, immunogenicity, and inflammation are some of the most significant [7,35,36]. The metallo-elastomer departs from traditional materials and offers vascular grafts ample control of degradation rates, mechanical properties, and biological functions by varying metal ion types, metal/ligand ratios, and ligand density [21]. We started with the selection of metal ions from Zn^{2+}, Fe^{3+}, and Cu^{2+}, all of which offer sufficient mechanical strength. Zn^{2+} is known to be antiatherogenic and antioxidative. Zn^{2+} could also support endothelial membrane stability and prevent thrombosis [37]. Fe^{3+} produces the most elastic material of this group [21]. Cu^{2+} is known to promote angiogenesis and the migration and proliferation of endothelial cells [38]. Cu ions upregulates VEGF and fibroblast growth factor 1 (FGF1) expressions [39], stabilizes hypoxia-inducible factor 1-alpha (HIF-1α) [40], activates angiogenin [41], and participates in a range of other pathways related to angiogenesis [42]. Zn-PAS degrades quickly [21], while Fe-PAS and Cu-PAS degrade more slowly. With respect to mechanical properties, Fe-PAS shows remarkable toughness, while Zn-PAS and Cu-PAS are more ductile, (Fig. 1c). The rapid dilation of Zn-PAS grafts after two weeks indicated compromised structural integrity. The moderate success of Fe-PAS grafts emphasized the need to balance degradation kinetics and mechanical strength (Fig. 1d; Fig. S7, Supplementary Information). Cu-PAS grafts, with the slowest degradation and excellent elasticity, emerged as the most promising candidate and the focus for further experiments, as indicated by graft patency and minimal dilation after 8 weeks (Fig. 1d).

SEM images demonstrated uniform pore distribution and interconnectivity in Cu-PAS grafts (Fig. 2a), essential for optimal cell infiltration and nutrient exchange [43]. The graft's elasticity, evidenced by its ability to recover after repeated deformations (Fig. 2b, Fig. S8, Supplementary Information), is reminiscent of native blood vessels and likely important for the formation of elastic fibers [44]. Cu-PAS grafts were interposed into 26 Sprague Dawley rats' left common carotid arteries, with the contralateral artery as a control. Over a year, Cu-PAS grafts maintained a 76 % overall patency rate, with confluent neointima formation observed after 4 months (Fig. S9, Supplementary Information). Ultrasound confirmed stable blood flow and robust mechanical integrity throughout the 12-month period (Fig. 3), suggesting a direct correlation between graft stability, blood flow consistency, and long-term success of the graft.

Histological analysis reveals that Cu-PAS grafts gradually degrade and integrate with infiltrating cells and the tissues they form (Fig. 4a and b) [45]. By 8 and 12 months, these grafts transition towards being replaced by natural tissue (Fig. 4, Fig. S12, Supplementary Information). The grafts had significantly larger luminal areas and wall thickness than contralateral native carotids at all time points ($P < 0.001$, Fig. 4c–and d). We attributed this to two factors: 1, the graft was oversized as revealed by the ultrasound at day 4. And 2, The luminal dimensions of the native artery measured in H&E-stained sections would be smaller than that of the artery under physiological conditions because the artery was fixed unpressurized. The neoartery remodeling was guided by the Cu-PAS grafts as a template, which had a thicker wall. The thicker wall of these grafts arises from the limitation on the thinness of the PMMA template. Additionally, since the rate at which these grafts degrade *in vivo* remains unknown, we opt for a thicker wall in this study to decrease PMMA template defects and mitigate the risk of ruptures or dilation that might occur should the *in vivo* degradation be much faster than *in vitro*. As time progresses, it is expected that the wall thickness of the neoartery will decrease to the level of native arteries.

Cellular infiltration and organization within the grafts indicated successful integration (Fig. 4e, Fig. S13, Supplementary Information). The transition from prominent macrophage presence to tissue akin to the native artery by 12 months reaffirmed the biocompatibility of Cu-PAS grafts, suggesting a reduced immunogenicity [18]. The inflammatory response, predominantly regulated by macrophages, is essential for tissue remodeling and integration of the grafts [46]. Variations in $CD68^{+}$ cell distribution correlated with Cu-PAS degradation stages, underscoring the macrophage-mediated remodeling (Fig. 5). Macrophages exhibited high plasticity, allowing them to differentiate into both type I (M1) and type II (M2) macrophages [47]. The balance between M1 and M2 macrophages is crucial for inflammatory modulation and tissue healing [48]. Our findings of a high M2/M1 ratio, particularly after 4 months, suggest a predominantly anti-inflammatory environment conducive to graft integration and tissue remodeling. Ensuring graft endothelialization is key to preventing clotting [49]. A thin endothelial layer was present at the luminal surface of the Cu-PAS grafts as early as 1 month, which became thicker by 4 months and sustained at 12 months (Fig. 6a and b, Fig. S15, Supplementary Information), signified the heparin-coated Cu-PAS grafts' potential to provide a non-thrombogenic luminal surface.

The ECs' native-like morphology and arrangement indicated a functional adaptation of the graft endothelium to blood flow, crucial for long-term graft patency [36]. Similarly, the organized presence of smooth muscle cell (SMC) markers from 4 months on reflected the structural and functional maturation of the graft (Fig. 6d), akin to natural arteries [50]. The vascular extracellular matrix (ECM) serves as a foundation for both cellular and mechanical functions [51]. Our findings illustrated that the ECM in Cu-PAS grafts were comparable to native carotids over the 12-month period (Fig. 4; Fig. 7; Figs. S18 and S19, Supplementary Information), with a consistent presence of collagen types I and III, and elastin arrangement indicative of arterial tissue regeneration [52]. No calcification was observed, highlighting biocompatibility [53]. Mechanical tests for the 12-month explants revealed that the neo-artery showed similarity to native arteries in circumferential pressure-strain curves, suggesting graft maturation over time (Fig. 7c) [54]. The explants withstood arterial pressure (Fig. 7e) but were less compliant after 12 months ($P < 0.05$, Fig. 7d), possibly due to an imbalance in collagen and elastin or incomplete maturation of these elements [55].

The proteomics insights offer a deeper dive into the remodeling processes. The identified proteins, especially fibrillar collagens, elastin, proteoglycans, and glycoproteins (All Proteins spreadsheet, Supplementary Information 2), matched those in native arterial ECM, contributing to both mechanical integrity and vital cellular functions for vascular regeneration [56]. The presence of integrins, known mediators of cell-ECM interactions [57], further emphasized the graft's functional restoration potential. Protein-protein interaction analysis, gene ontology enrichment analysis, and pathways analysis (Fig. 8) revealed increased abundance proteins crucial for cell adhesion, migration, signaling, ECM organization, smooth muscle contraction, tissue development, and tissue remodeling [58,59], which are vital for neoartery regeneration and vascular biology. In contrast, decreased abundance proteins appeared to disrupt neoartery structural integrity and ECM composition [60], potentially leading to anti-thrombotic events and size-reducing of the neoartery. Overall, the proteomics analysis unveiled a complex orchestration of pathways and processes that collectively contribute to neoartery regeneration. From protein interactions to functional pathways, these biological processes, when harmonized, promote artery growth and functional restoration [61].

The presence of ECM proteins in the neo-artery resembles that of native arteries. This supports essential vascular cell functions and differentiation while bearing the majority of load in the arterial circulation. This kind of remodeling went a step further than integration, as the resultant neo-artery functions like a native artery. Moreover, proteomics analysis of the neoartery yielded more insights on protein expression. This analysis not only indicated the biological similarity between the graft and native tissue but also provided a platform to delve deeper into understanding the complex biological processes and pathways underpinning the graft's performance. It should be noted that the graft's wall thickness hadn't fully returned to native artery levels, and the compliance is lower. The ongoing remodeling process, extending beyond 12

months with 5 % material remaining, was on the longer end relative to other resorbable vascular grafts [18]. However, others' work [20] and our prior studies using PGS grafts demonstrated that polyester vascular grafts degraded faster in large animals such as sheep than in rats. In rat carotid artery interpositions using PGS grafts, PGS was still present after three months [18]. However, when the PGS grafts were scaled-up and applied to the sheep carotid interpositions model, the PGS material nearly completely degraded within 15 days [19]. A nanofiber vascular graft degraded significantly faster in sheep than in rats, in both the arterial and the venous circulations. Thus, we designed the Cu-PAS grafts with a relatively slow degradation rate in rats, aiming for a multi-month degradation window in large animals and potentially future clinical translation.

There are reports highlighting the significant role of a conducive scaffold environment in the vascular regeneration process, including the degradation behavior, accumulation of ECs and SMCs, and other cellular dynamics on the outer surfaces of the grafts. For example, Wang et al. reported rapid regeneration of a neoartery with elastic lamellae in a tropoelastin-PGS graft [62]. We would like to note that there are differences in the material composition and structure of the grafts. The porous Cu-PAS grafts facilitate a different pattern of cell infiltration and tissue integration compared to the non-porous tropoelastin-PGS grafts. This structural variation likely influences the scaffold's mechanical properties, degradation rates, and the subsequent cellular and extracellular matrix organization. Moreover, the tropoelastin-PGS grafts utilize the elastic properties of tropoelastin and the biodegradability of PGS to promote elastin organization, whereas the Cu-PAS grafts feature copper's angiogenic properties within an elastic and biodegradable matrix.

A limitation of this study is that we didn't examine the release of Cu^{2+} ions *in vivo*. Excessive Cu^{2+} will cause cellular damage [30]. However, metal ion toxicity primarily arises from free metal ions. The total amount of Cu^{2+} ions in Cu-PAS graft is very low (13.46 μg Cu^{2+} per 1 mg Cu-PAS), Furthermore, the metal ions are chelated to the polymeric ligands, and not in the free state. In fact, a common therapy for metal ion toxicity is the administration of ligands. Moreover, organisms possess intricate copper homeostasis mechanisms that regulate copper uptake, distribution, sequestration, and export, involving metal-responsive transcription factors like MTF-1 [63].

In the future, we aim to address the graft dilation issue observed in Cu-PAS grafts. This could involve refining the graft material or introducing reinforcement mechanisms. For instance, a potential approach is to utilize a combination of Fe^{3+} and Cu^{2+} as crosslinkers to prepare Fe/Cu-PAS elastomers, with the goal of improving elasticity. To ensure consistent biocompatibility, we plan to integrate comprehensive immunological studies to assess potential immune reactions throughout the graft's lifecycle. As the graft undergoes remodeling, it would be beneficial to conduct mechanical tests and proteomics studies. This information will further guide the optimization of the grafts. As is the case with other cell-free vascular grafts under development, Cu-PAS graft is likely to be provided off-the-shelf. We notice little change to our grafts stored under vacuum at room temperature after 1.5 years. Further tests will assess the impact of storage under other conditions.

5. Conclusion

This study introduces an innovative biodegradable elastomer, Cu-PAS, as a new material to build vascular grafts. The novel material platform offers facile customization options for degradation rates, mechanical properties, and potentially biological functions, important parameters to adjust as the grafts advance from small animal to large animal models and eventually human clinical applications. Utilizing a rat carotid artery interposition model, we observed the transformation of a cell-free synthetic grafts into an autologous host vascular conduit over 12 months. These grafts displayed good patency rates. The grafts were repopulated with host cells rapidly. The exogenous polymer degraded gradually as part of the host remodeling process. They underwent consistent compositional changes without exhibiting signs of stenosis or aneurysm. Future work will examine how the transformation occurs in large animals such as sheep.

CRediT authorship contribution statement

Ying Grace Chen: Writing – review & editing, Writing – original draft, Visualization, Validation, Project administration, Methodology, Investigation, Formal analysis, Data curation, Conceptualization. **Catia Dombaxe:** Writing – review & editing, Methodology, Formal analysis, Data curation. **Anthony Richard D'Amato:** Writing – review & editing, Visualizaiton, Methodology, Formal analysis, Dara curation. **Simon Van Herck:** Writing – review & editing, Formal analysis, Data curation. **Halle Welch:** Visualization, Formal analysis, Data curation. **Qin Fu:** Writing – review & editing, Methodology, Formal analysis, Data curation. **Sheng Zhang:** Writing – review & editing, Methodology, Formal analysis, Data curation. **Yadong Wang:** Writing – review & editing, Supervision, Resources, Project administration, Methodology, Investigation, Funding acquisition, Formal analysis, Conceptualization.

Declaration of competing interest

The authors declare that they have no known competing financial interests or personal relationships that could have appeared to influence the work reported in this paper.

Data availability

Data will be made available on request.

Acknowledgements

This work was supported by NIH grant #R01HL159427. This work uses the Cornell Center for Materials Research Shared Facilities which are supported through the NSF MRSEC program (DMR-1719875) and the Cornell University NMR Facility, supported by the NSF MRI award CHE-1531632. This work made use of the Cornell Institute of Biotechnology's BRC Imaging Facility (RRID:SCR_021741), with NYSTEM (C029155) and NIH (S10OD018516) funding for the shared Zeiss LSM880 confocal/multiphoton microscope. NIH SIG grant 1S10 OD017992-01 funding for the Orbitrap Fusion mass spectrometer. All work with live animals followed a protocol (protocol # 2017–0118) approved by the Cornell University Institutional Animal Care and Use Committee.

Appendix A. Supplementary data

Supplementary data to this article can be found online at https://doi.org/10.1016/j.biomaterials.2024.122598.

References

[1] R. Khosravi, C.A. Best, R.A. Allen, C.E. Stowell, E. Onwuka, J.J. Zhuang, Y.-U. Lee, T. Yi, M.R. Bersi, T. Shinoka, Long-term functional efficacy of a novel electrospun poly (glycerol sebacate)-based arterial graft in mice, Ann. Biomed. Eng. 44 (8) (2016) 2402–2416.
[2] B.C. Isenberg, C. Williams, R.T. Tranquillo, Small-diameter artificial arteries engineered in vitro, Circ. Res. 98 (1) (2006) 25–35.
[3] S. Koch, T.C. Flanagan, J.S. Sachweh, F. Tanios, H. Schnoering, T. Deichmann, V. Ellä, M. Kellomäki, N. Gronloh, T. Gries, Fibrin-polylactide-based tissue-engineered vascular graft in the arterial circulation, Biomaterials 31 (17) (2010) 4731–4739.
[4] N. Tai, H. Salacinski, A. Edwards, G. Hamilton, A. Seifalian, Compliance properties of conduits used in vascular reconstruction, Br. J. Surg. 87 (11) (2000) 1516–1524.
[5] M. Neufurth, X. Wang, E. Tolba, B. Dorweiler, H.C. Schröder, T. Link, B. Diehl-Seifert, W.E. Müller, Modular small diameter vascular grafts with bioactive functionalities, PLoS One 10 (7) (2015) e0133632.
[6] L. Xue, H.P. Greisler, Biomaterials in the development and future of vascular grafts, J. Vasc. Surg. 37 (2) (2003) 472–480.

[7] C.E. Stowell, Y. Wang, Quickening: Translational design of resorbable synthetic vascular grafts, Biomaterials 173 (2018) 71–86.
[8] H. Kurobe, M.W. Maxfield, S. Tara, K.A. Rocco, P.S. Bagi, T. Yi, B. Udelsman, Z. W. Zhuang, M. Cleary, Y. Iwakiri, Development of small diameter nanofiber tissue engineered arterial grafts, PLoS One 10 (4) (2015) e0120328.
[9] S. Tara, H. Kurobe, K.A. Rocco, M.W. Maxfield, C.A. Best, T. Yi, Y. Naito, C. K. Breuer, T. Shinoka, Well-organized neointima of large-pore poly (L-lactic acid) vascular graft coated with poly (L-lactic-co-ε-caprolactone) prevents calcific deposition compared to small-pore electrospun poly (L-lactic acid) graft in a mouse aortic implantation model, Atherosclerosis 237 (2) (2014) 684–691.
[10] T. Yokota, H. Ichikawa, G. Matsumiya, T. Kuratani, T. Sakaguchi, S. Iwai, Y. Shirakawa, K. Torikai, A. Saito, E. Uchimura, In situ tissue regeneration using a novel tissue-engineered, small-caliber vascular graft without cell seeding, J. Thorac. Cardiovasc. Surg. 136 (4) (2008) 900–907.
[11] W. Zhao, J. Li, K. Jin, W. Liu, X. Qiu, C. Li, Fabrication of functional PLGA-based electrospun scaffolds and their applications in biomedical engineering, Mater. Sci. Eng. C 59 (2016) 1181–1194.
[12] S. de Valence, J.-C. Tille, D. Mugnai, W. Mrowczynski, R. Gurny, M. Möller, B. H. Walpoth, Long term performance of polycaprolactone vascular grafts in a rat abdominal aorta replacement model, Biomaterials 33 (1) (2012) 38–47.
[13] Y.M. Kang, S.H. Lee, J.Y. Lee, J.S. Son, B.S. Kim, B. Lee, H.J. Chun, B.H. Min, J. H. Kim, M.S. Kim, A biodegradable, injectable, gel system based on MPEG-b-(PCL-ran-PLLA) diblock copolymers with an adjustable therapeutic window, Biomaterials 31 (9) (2010) 2453–2460.
[14] D. Zhi, Q. Cheng, A.C. Midgley, Q. Zhang, T. Wei, Y. Li, T. Wang, T. Ma, M. Rafique, S. Xia, Mechanically reinforced biotubes for arterial replacement and arteriovenous grafting inspired by architectural engineering, Sci. Adv. 8 (11) (2022) eabl3888.
[15] Y. Pan, X. Zhou, Y. Wei, Q. Zhang, T. Wang, M. Zhu, W. Li, R. Huang, R. Liu, J. Chen, Small-diameter hybrid vascular grafts composed of polycaprolactone and polydioxanone fibers, Sci. Rep. 7 (1) (2017) 3615.
[16] J.V. Cauich-Rodríguez, L.H. Chan-Chan, F. Hernandez-Sánchez, J.M. Cervantes-Uc, Degradation of polyurethanes for cardiovascular applications, Advances in biomaterials science and biomedical applications (2013) 51–82.
[17] Y. Wang, G.A. Ameer, B.J. Sheppard, R. Langer, A tough biodegradable elastomer, Nat. Biotechnol. 20 (6) (2002) 602–606.
[18] K.-W. Lee, P.S. Gade, L. Dong, Z. Zhang, A.M. Aral, J. Gao, X. Ding, C.E. Stowell, M. U. Nisar, K. Kim, A biodegradable synthetic graft for small arteries matches the performance of autologous vein in rat carotid arteries, Biomaterials 181 (2018) 67–80.
[19] C.E. Stowell, X. Li, M.H. Matsunaga, C.B. Cockreham, K.M. Kelly, J. Cheetham, E. Tzeng, Y. Wang, Resorbable vascular grafts show rapid cellularization and degradation in the ovine carotid, Journal of tissue engineering and regenerative medicine 14 (11) (2020) 1673–1684.
[20] T. Fukunishi, C.S. Ong, P. Yesantharao, C.A. Best, T. Yi, H. Zhang, G. Mattson, J. Boktor, K. Nelson, T. Shinoka, Different degradation rates of nanofiber vascular grafts in small and large animal models, Journal of tissue engineering and regenerative medicine 14 (2) (2020) 203–214.
[21] Y. Chen, P.G. Miller, X. Ding, C.E. Stowell, K.M. Kelly, Y. Wang, Chelation crosslinking of biodegradable elastomers, Adv. Mater. 32 (43) (2020) 2003761.
[22] S. Ramakrishna, J. Mayer, E. Wintermantel, K.W. Leong, Biomedical applications of polymer-composite materials: a review, Compos. Sci. Technol. 61 (9) (2001) 1189–1224.
[23] L. Zhen, S.A. Creason, F.I. Simonovsky, J.M. Snyder, S.L. Lindhartsen, M. M. Mecwan, B.W. Johnson, J. Himmelfarb, B.D. Ratner, Precision-porous polyurethane elastomers engineered for application in pro-healing vascular grafts: Synthesis, fabrication and detailed biocompatibility assessment, Biomaterials 279 (2021) 121174.
[24] X. Qiu, B.L.-P. Lee, X. Ning, N. Murthy, N. Dong, S. Li, End-point immobilization of heparin on plasma-treated surface of electrospun polycarbonate-urethane vascular graft, Acta Biomater. 51 (2017) 138–147.
[25] W.C. Chen, Z. Wang, M.A. Missinato, D.W. Park, D.W. Long, H.-J. Liu, X. Zeng, N. A. Yates, K. Kim, Y. Wang, Decellularized zebrafish cardiac extracellular matrix induces mammalian heart regeneration, Sci. Adv. 2 (11) (2016) e1600844.
[26] Y. Yang, E. Anderson, S. Zhang, Evaluation of six sample preparation procedures for qualitative and quantitative proteomics analysis of milk fat globule membrane, Electrophoresis 39 (18) (2018) 2332–2339.
[27] A. Zougman, P.J. Selby, R.E. Banks, Suspension trapping (STrap) sample preparation method for bottom-up proteomics analysis, Proteomics 14 (9) (2014), 1006-1000.
[28] R.M. Harman, M.K. He, S. Zhang, G.R. Van de Walle, Plasminogen activator inhibitor-1 and tenascin-C secreted by equine mesenchymal stromal cells stimulate dermal fibroblast migration in vitro and contribute to wound healing in vivo, Cytotherapy 20 (8) (2018) 1061–1076.
[29] Y. Chen, N. Kawazoe, G. Chen, Preparation of dexamethasone-loaded biphasic calcium phosphate nanoparticles/collagen porous composite scaffolds for bone tissue engineering, Acta Biomater. 67 (2018) 341–353.
[30] K. Balamurugan, W. Schaffner, Copper homeostasis in eukaryotes: teetering on a tightrope, Biochim. Biophys. Acta Mol. Cell Res. 1763 (7) (2006) 737–746.
[31] G.R. Whittell, M.D. Hager, U.S. Schubert, I. Manners, Functional soft materials from metallopolymers and metallosupramolecular polymers, Nat. Mater. 10 (3) (2011) 176.
[32] H.-H.G. Song, R.T. Rumma, C.K. Ozaki, E.R. Edelman, C.S. Chen, Vascular tissue engineering: progress, challenges, and clinical promise, Cell Stem Cell 22 (3) (2018) 340–354.
[33] N. Thottappillil, P.D. Nair, Scaffolds in Vascular Regeneration: Current Status, Vascular Health and Risk Management, 2015, pp. 79–91.
[34] Y. Matsuzaki, K. John, T. Shoji, T. Shinoka, The evolution of tissue engineered vascular graft technologies: from preclinical trials to advancing patient care, Appl. Sci. 9 (7) (2019) 1274.
[35] L. Soffer, X. Wang, X. Zhang, J. Kluge, L. Dorfmann, D.L. Kaplan, G. Leisk, Silk-based electrospun tubular scaffolds for tissue-engineered vascular grafts, J. Biomater. Sci. Polym. Ed. 19 (5) (2008) 653–664.
[36] F.O. Obiweluozor, G.A. Emechebe, D.-W. Kim, H.-J. Cho, C.H. Park, C.S. Kim, I. S. Jeong, Considerations in the development of small-diameter vascular graft as an alternative for bypass and reconstructive surgeries: a review, Cardiovascular Engineering and Technology 11 (2020) 495–521.
[37] P.K. Bowen, E.R. Shearier, S. Zhao, R.J. Guillory, F. Zhao, J. Goldman, J. W. Drelich, Biodegradable metals for cardiovascular stents: from clinical concerns to recent Zn-Alloys, Adv. Healthcare Mater. 5 (10) (2016) 1121–1140.
[38] G.f. Hu, Copper stimulates proliferation of human endothelial cells under culture, J. Cell. Biochem. 69 (3) (1998) 326–335.
[39] E.D. Harris, A requirement for copper in angiogenesis, Nutr. Rev. 62 (2) (2004) 60–64.
[40] F. Martin, T. Linden, D.r.M. Katschinski, F. Oehme, I. Flamme, C. K. Mukhopadhyay, K. Eckhardt, J. Troger, S. Barth, G. Camenisch, Copper-dependent activation of hypoxia-inducible factor (HIF)-1: implications for ceruloplasmin regulation, Blood 105 (12) (2005) 4613–4619.
[41] F. Soncin, J.-D. Guitton, T. Cartwright, J. Badet, Interaction of human angiogenin with copper modulates angiogenin binding to endothelial cells, Biochem. Biophys. Res. Commun. 236 (3) (1997) 604–610.
[42] S.A. Lowndes, A.L. Harris, The role of copper in tumour angiogenesis, J. Mammary Gland Biol. Neoplasia 10 (2005) 299–310.
[43] Y. Chen, J. Wang, X. Zhu, Z. Tang, X. Yang, Y. Tan, Y. Fan, X. Zhang, Enhanced effect of β-tricalcium phosphate phase on neovascularization of porous calcium phosphate ceramics: in vitro and in vivo evidence, Acta Biomater. 11 (2015) 435–448.
[44] S. Greenwald, C. Berry, Improving vascular grafts: the importance of mechanical and haemodynamic properties, J. Pathol. 190 (3) (2000) 292–299.
[45] M. Prakasam, J. Locs, K. Salma-Ancane, D. Loca, A. Largeteau, L. Berzina-Cimdina, Biodegradable materials and metallic implants—a review, J. Funct. Biomater. 8 (4) (2017) 44.
[46] M. Zhu, Y. Wu, W. Li, X. Dong, H. Chang, K. Wang, P. Wu, J. Zhang, G. Fan, L. Wang, Biodegradable and elastomeric vascular grafts enable vascular remodeling, Biomaterials 183 (2018) 306–318.
[47] N. Jetten, S. Verbruggen, M.J. Gijbels, M.J. Post, M.P. De Winther, M.M. Donners, Anti-inflammatory M2, but not pro-inflammatory M1 macrophages promote angiogenesis in vivo, Angiogenesis 17 (2014) 109–118.
[48] N. Wang, H. Liang, K. Zen, Molecular mechanisms that influence the macrophage M1–M2 polarization balance, Front. Immunol. 5 (2014) 614.
[49] D. Radke, W. Jia, D. Sharma, K. Fena, G. Wang, J. Goldman, F. Zhao, Tissue engineering at the blood-contacting surface: a review of challenges and strategies in vascular graft development, Adv. Healthcare Mater. 7 (15) (2018) 1701461.
[50] R.W. Thompson, S. Liao, J.A. Curci, Vascular smooth muscle cell apoptosis in abdominal aortic aneurysms, Coron. Artery Dis. 8 (10) (1997) 623–632.
[51] G.E. Davis, D.R. Senger, Endothelial extracellular matrix: biosynthesis, remodeling, and functions during vascular morphogenesis and neovessel stabilization, Circ. Res. 97 (11) (2005) 1093–1107.
[52] F.H. Silver, I. Horvath, D.J. Foran, Viscoelasticity of the vessel wall: the role of collagen and elastic fibers, Crit. Rev. Biomed. Eng. 29 (3) (2001).
[53] R.I. Mehta, A.K. Mukherjee, T.D. Patterson, M.C. Fishbein, Pathology of explanted polytetrafluoroethylene vascular grafts, Cardiovasc. Pathol. 20 (4) (2011) 213–221.
[54] Z.H. Syedain, L.A. Meier, J.W. Bjork, A. Lee, R.T. Tranquillo, Implantable arterial grafts from human fibroblasts and fibrin using a multi-graft pulsed flow-stretch bioreactor with noninvasive strength monitoring, Biomaterials 32 (3) (2011) 714–722.
[55] J. Szafron, R. Khosravi, J. Reinhardt, C. Best, M. Bersi, T. Yi, C. Breuer, J. Humphrey, Immuno-driven and mechano-mediated neotissue formation in tissue engineered vascular grafts, Ann. Biomed. Eng. 46 (2018) 1938–1950.
[56] J.E. Wagenseil, R.P. Mecham, Vascular extracellular matrix and arterial mechanics, Physiol. Rev. 89 (3) (2009) 957–989.
[57] P.C. Brooks, Role of integrins in angiogenesis, Eur. J. Cancer 32 (14) (1996) 2423–2429.
[58] H.R. Bender, G.E. Campbell, P. Aytoda, A.H. Mathiesen, D.M. Duffy, Thrombospondin 1 (THBS1) promotes follicular angiogenesis, luteinization, and ovulation in primates, Front. Endocrinol. 10 (2019) 727.
[59] K. Minamiguchi, H. Kumagai, T. Masuda, M. Kawada, M. Ishizuka, T. Takeuchi, Thiolutin, an inhibitor of HUVEC adhesion to vitronectin, reduces paxillin in HUVECs and suppresses tumor cell-induced angiogenesis, Int. J. Cancer 93 (3) (2001) 307–316.
[60] G. del Monte-Nieto, J.W. Fischer, D.J. Gorski, R.P. Harvey, J.C. Kovacic, Basic biology of extracellular matrix in the cardiovascular system, part 1/4: JACC focus seminar, J. Am. Coll. Cardiol. 75 (17) (2020) 2169–2188.
[61] L. Antonova, A. Kutikhin, V. Sevostianova, A. Lobov, E. Repkin, E. Krivkina, E. Velikanova, A. Mironov, R. Mukhamadiyarov, E. Senokosova, Controlled and synchronised vascular regeneration upon the implantation of iloprost-and cationic

amphiphilic drugs-conjugated tissue-engineered vascular grafts into the ovine carotid artery: a proteomics-empowered study, Polymers 14 (23) (2022) 5149.
[62] Z. Wang, S.M. Mithieux, H. Vindin, Y. Wang, M. Zhang, L. Liu, J. Zbinden, K. M. Blum, T. Yi, Y. Matsuzaki, Rapid regeneration of a neoartery with elastic lamellae, Adv. Mater. 34 (47) (2022) 2205614.
[63] J.C. Rutherford, A.J. Bird, Metal-responsive transcription factors that regulate iron, zinc, and copper homeostasis in eukaryotic cells, Eukaryot. Cell 3 (1) (2004) 1–13.